Action 1.2: Impact study

Report on experimental and numerical modelling

Deliverables:

Study of processes at the scale of a monopile

Parameterisation study of local processes

Environmental impact assessment at regional scale

OFELIA - Deliverable 1.2

June 14, 2015

Contents

I

Preface

The deliverables of the OFELIA project were addressed by cooperation between the three project partners. Each institution worked to its strengths, in terms of facilities and expertise. Plymouth University made use of the coastal basin to study the wake structure downstream of the pile, and the effect of changing wave angle. The University of Le Havre used their wave flume and PIV system to make detailed velocity measurements near the pile base under different wave conditions. Caen University contributed to both numerical and physical aspects of the project. Physical modelling with sediments took place in their wave-current flume. Numerical modelling was carried out using the MARS3D regional hydro-sedimentary model. This document summarises the work carried out during the project, and demonstrates how the deliverables were met.

I.1 Study of processes at the scale of a monopile

Several different processes were studied at the monopile scale. Detailed measurements were made of the Hydrodynamics in the vicinity of the pile using both PIV and ADV equipment (sections V.2, VII.2.2). These can be compared to numerical results showing surface and near-bed velocity and barotropic vorticity around a monopile (section VI.3.1.2). The streamwise component of velocity downstream of the modelled monopile is in good agreement with experimental measurements.

Detailed experimental measurements were made of turbulence in the pile wake under a range of model conditions (section VII.2.1). Flow structures generated along the pile and also at the lee side, were detected with PIV measurements (section V.3.2). Velocity measurements made during scour hole development allowed examination of the scour hole's influence on turbulence (section III.6).

Scour hole development was studied both experimentally and numerically. Detailed bed profiles of mobile bed under varying input conditions were collected during laboratory experiments (section III.6). Numerical modelling produced estimations of the horizontal distribution of bed shear stress, suspended sediment concentration and bed thickness (sections VI.3.1, VI.3.2). The patterns of bed thickness downstream of a monopile shown by the experimental and numerical work are in close agreement.

Interaction between waves and current was examined in a number of ways. Velocity profiles upstream and downstream of the pile were compared to undisturbed conditions, under waves and opposing currents (section III.6.1). A synchronisation phenomenon was identified, where resonant effects occur between waves and Von Karman vortices (section IV.3).

I.2 Parameterisation study of local processes

Study of the processes described above led to several novel parameterisations. Using experimental data, two new parameters were developed to describe the pile wake (section VII.2.3). The Turbulence Recovery Lengthscale and Relative Excess Turbulence allow the distribution of turbulence downstream of a pile to be predicted from its diameter and the mean undisturbed flow velocity.

Experimental measurements of scour hole development have been compared to existing formulae (section III.6.3). The results will allow parameterisation of other scour hole characteristics, such as volume, diameter and shape.

From resonance experiments, the threshold conditions for onset of synchronisation were identified (Figure IV.2). This will aid prediction of the enhanced velocity fluctuations occurring during resonance.

Two strategies were tested to represent a monopile in the numerical model: (a) an explicit resolution of the monopile in the mesh and (b) a subgrib parametrization of the monopile's effect on hydrodynamics, by adding drag force terms in momentum equations and source terms of turbulence in k-epsilon turbulence model equation. The first technique is the reference and gives results in agreement with literature and experimental data (velocity, turbulence). Results obtained with the parametrization are compared to results from the explicit method and both approaches show similar modifications of bed shear stress, suspended sediments concentration and bed thickness due to the monopile (section VI.2).

I.3   Environmental impact assessment at regional scale

Experimentally derived turbulence parameterisations were used to identify the spatial extent of a monopile's influence on turbulence. They have also been used to examine the likely cumulative effect on turbulence of successive foundations in an array (sections VII.3.3, VII.4). These parameterisations are suitable for environmental impact assessment of future sites.

Regional scale modelling has been conducted on the future site of Courseulles wind farm (Calvados, France) with a multigrid method. The regional impact of 4 piles are numerically modelled using the explicit method and the sub-grid parametrization (VI.3.2). Wake effect and piles interactions have been observed with modifications of the pattern of velocity and sediment transport concentration around the monopile located downstream in the array. Small modifications of velocity ($< 10\%$) around this downstream monopile can lead to stronger modifications of suspended sediment concentration at this location.

I.4

This brochure represents a brief summary of the work carried out during the project. For an in-depth account of the work and findings, please consult the published outputs from the project listed overleaf.

II

List of Publications

The following publications were produced during the project:

II.1   Journal Publications

[1] M. I. Garca-Hermosa, G. Perret and J. Brossard. Characterisation of flow structures in the vicinity of an offshore wind farm monopile under waves. *In preparation.*

[2] H. Gunnoo, N. Abcha and A.B. Ezersky. Frequency lock-in and phase synchronization of vortex shedding behind circular cylinder due to surface waves. *Under Review - Physics of Fluids*

[3] A. Rivier, A. C. Bennis, G. Pinon, V. Magar and M. Gross. Parametrization of wind turbine impacts on hydrodynamics and sediment transport. *In preparation.*

[4] C. Rogan, J. Miles, D. Simmonds and G. Iglesias. The turbulent wake of a monopile foundation. *Under Review - Renewable Energy.*

II.2   Conference Proceedings

[1] M I García-Hermosa, J Brossard, Z Cohen, G Perret. Experimental characterisation of wave induced flow fields due to an offshore wind farm mast. In *Proceedings of the 1st International Conference on Renewable Energies Offshore*, Lisbon, 2014

[2] M I García-Hermosa, N Abcha, J Brossard, A-C Bennis, A Ezersky, M Gross, G Iglesias, V Magar, J Miles, D Mouazé, G Perret, G Pinon, A Rivier, C Rogan, D Simmonds. Characterisation of impacts on the environment of an idealised offshore wind farm foundation, under waves and the combination of waves and currents. In *Proceedings of the General Assembly of the European Geosciences Union*, Vienna, 2015.

[3] H Gunnoo, N Abcha, D Mouazé and A Ezersky. Laboratory simulation of resonance amplification of the hydrodynamic fields in the vicinity of wind farm masts. In *Proceedings of the 1st International Conference on Renewable Energies Offshore*, Lisbon, 2014

[4] V Magar, N Abcha, A C Bennis, J Brossard, D Conley and E Ellis. Laboratory-Scale Environmental Impact Assessment of a Monopile Foundation under Different Wave Conditions. In *Proceedings of European Wind Energy Association Offshore conference*, Frankfurt, 2013.

[5] A Rivier, A C Bennis, G Pinon, M Gross and V Magar. Modélisation numérique régionale de l'impact des éoliennes offshore sur l'hydrodynamique et le transport sédimentaire. In *Proceedings of the 14th Journées de l'hydrodynamique*, Val de Reuil, 2014.

[6] A Rivier, A C Bennis, G Pinon, M Gross and V Magar. Regional numerical modelling of offshore monopile wind turbine impacts on hydrodynamics and sediment transport. In *Proceedings of the 1st International Conference on Renewable Energies Offshore*, Lisbon, 2014.

[7] C Rogan, J Miles, D Simmonds and G Iglesias. Regional numerical modelling of offshore monopile wind turbine impacts on hydrodynamics and sediment transport In *Proceedings of the 1st International Conference on Renewable Energies Offshore*, Lisbon, 2014

II.3   Poster Presentations

[1] V. Magar, N. Abcha, A. C. Bennis, J. Brossard, D.C. Conley, E. Ellis, A. Ezersky, D. Greaves, M.S. Gross, G. Iglesias, K. Littlewood, J. Miles, D. Mouaze, G. Perret, G. Pinon, D. Simmonds Laboratory-Scale Environmental Impact Assessment of a Monopile Foundation under Different Wave Conditions. Poster presented to the *1st European Wind Energy Association Offshore Conference* Frankfurt, 2013

[2] Aurélie Rivier, Anne-Claire Bennis, Grégory Pinon, Vanesa Magar, and Markus Gross. Assessment by regional modelling of the impact of monopile foundations on the hydrodynamics and sediment transport: case of Courseulles-sur-Mer (France) wind farm. Poster presented to the *General Assembly of the European Geosciences Union* Vienna, 2015

[3] C. Rogan, A. C. Bennis, I. García-Hermosa, G. Iglesias, V. Magar, J. Miles, G. Perret, G. Pinon, A. Rivier, D. Simmonds Physical and Numerical Modelling of Hydrodynamics and Sediment Transport at Monopile Foundations. Poster presented to the *1st Partnership for Research in Marine Renewable Energy Conference* Plymouth, 2014

II.4   Masters Dissertations

[1] T W Clyde. An investigation into the flow dynamics and bed load transport rate around a cylindrical pile in wave and current conditions of Scroby Sands and Thanet offshore wind farm sites. A dissertation submitted in partial fulfilment of the degree of MSc Marine Renewable Energy, Plymouth University, September 2013.

[2] Z Cohen. Characterization of the flow around offshore wind turbine. A dissertation submitted in partial fulfilment of the degree of Master in Renewable Energy and Civil Engineering, University of Le Havre, September 2014.

[3] M Dight. Investigation into the change in hydrodynamic conditions and environmental impacts caused by the introduction of a wind turbine monopile to the marine environment. A dissertation submitted in partial fulfilment of the degree of MSc Environmental Consultancy, Plymouth University, September 2013.

[4] J Greene. OFELIA Analysing the Hydrodynamic Impacts of Offshore Monopile Foundations. A dissertation submitted in partial fulfilment of the degree of MSc Coastal Engineering, Plymouth University, September 2013.

[5] H Gunnoo. Laboratory simulation of resonance amplification of the hydrodynamic fields in the vicinity of wind farm masts A dissertation submitted in partial fulfilment of the degree of Master in Renewable Energy and Civil Engineering, University of Le Havre, September 2014.

[6] S Neill. An investigation of downstream and localised turbulent kinetic energies around a monopile structure in combined waves and currents. A dissertation submitted in partial fulfilment of the degree of MSc in Coastal Engineering, Plymouth University, September 2014.

[7] R Quirke. Assessment of the impacts of offshore wind farm monopiles on bed shear-stress. A dissertation submitted in partial fulfilment of the degree of MSc in Coastal Engineering, Plymouth University, September 2014.

[8] K Sawant Hydrodynamic impact study of wave-foundation interaction in offshore wind turbine farm. A dissertation submitted in partial fulfilment of the degree of Master in Renewable Energy and Civil Engineering, University of Le Havre, April 2015.

III

Studying effects of combined wave and current in the vicinity of a scaled wind farm mast in a flume with a mobile beds

I. García-Hermosa, D. Mouazé, N. Abcha, A. Ezersky

III.1   Introduction

In the last ten years the requirements to generate energy from cleaner sources have pushed the renewable energy industry. National deadlines from the UK and France to achieve a percentage of their national energy consumption via renewable energies by 2020 resulted in the rapid expansion of the offshore wind energy. Currently offshore wind is the most advanced marine renewable device, this is the case as its technology was developed decades ago for inland resources.

The latest proposed developments are being pushed to deeper waters and have increased in scale and technical complexity with ever growing mast diameters and varying foundation options. The choice of mast foundation depends on factors such as: soil characteristics, water depth, hydrodynamic conditions and costs. These factors highlight the need to understand further the local and regional impacts of wind farm foundations.

The problem of cylinders under steady currents, wave conditions and a combination of waves and currents has been previously studied in [3], [1], [9], [10], [11] and [8]. The key processes are dominated by the boundary layer thickness, the Reynolds number; the pile diameter and the Keulegan-Carpenter number.

$$\text{Re} = \frac{U * D}{\nu} \tag{III.1}$$

where U is the free stream velocity, D is the cylinder diameter ν is the kinematic viscosity.

$$\text{KC} = \frac{U_m * T}{D} \tag{III.2}$$

where U_m is the bottom orbital velocity, T wave period and D the cylinder diameter.

Their relative importance and interactions informs about the relative dimensions of the flow separation processes around the cylinder, such as the horseshoe vortex and the lee wake vortices. These two have been identified to be key processes to understand scour around a vertical cylinder.

The experiments described in this report aim to study the interactions between a vertical cylinder, combined waves and currents and a mobile bed. The objective is to characterise the responses of the mobile bed and the changes in the hydrodynamics around the cylinder.

III.2 Laboratory set up

III.2.1 The flume

The flume site in the M2C is 18 m long, 0.51 m wide and 0.6 m in depth (Figure III.1). The offshore wind farm mast foundation was represented as a smooth transparent cylinder of 0.04 m diameter, equivalent to 4 m mast using Froude scaling with a scale of 1:100.

A paddle was present at one end of the flume and a spending beach, sat on honeycombs, was present at the opposite side of the flume. The honeycombs covered about 2/3 of the water depth in the flume and were placed to decrease the turbulence of the current. Said paddle was controlled by a computer system where long crested regular wave conditions were generated by inputting two variables: an amplitude (a) and a frequency (f) proxis for wave height and period. Measurements of velocity and free surface were carried out to ascertain the transfer function for the paddle and the given water depth. Velocity profiles and free surface measurements were carried out in the absence of the cylinder in order to characterise the hydrodynamics in the flume. The current was driven by a reversing pump system, the set up was such that the waves and currents were opposing, i.e. at 180°.

The cylinder of 0.04 m diameter, consisted of two parts, a base of approximately 0.05 m height, that was glued to the bottom of the flume; and another part that was placed on top of the base and was sitting on the top sides of the flume and was fixed to them. This system allowed the bed profile acquisition up- and downstream of the cylinder.

During the mobile bed tests, the water depth in the flume was set to 0.3 m, in the region of the mobile bed (a layer of 0.05 m) the water depth was 0.25 m.
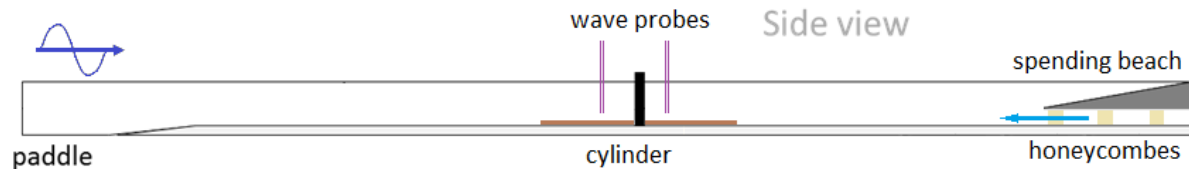

Figure III.1: Diagram of the laboratory set up

III.2.2 The flume floor and mobile bed

During the fixed bed experiments the bed of the flume was the normal glass bed. During the mobile bed experiments the floor of the flume was covered with a sand layer of 0.05 m thickness for approximately 2.6 to 2.5 m (Figure VI.2). The set up was such that the sand gently sloped at both sides up- and down-stream. From the full thickness of the layer (0.05 m) to the glass bed, for approximately 0.25 to 0.3 m (these side slopes are considered in the 2.5-2.6 m length of the sand layer) which corresponds to slopes of 1:4 to 1:6 or approximately 14 to 9°. Therefore the stretch of flat sand layer was about 2 m.

The characteristics of the sand used are shown in Figure VI.3. The characteristic grain size of the sand sample was $d_{50} = 0.153$ mm.

III.2.3 The measurements

Wave probes were used to acquire the variations in free surface. Measurements were made with three probes during estimate of the transfer function [6] and calibration of the flume conditions. Two probes were used to acquire free surface measurements during the tests from up- and down-stream from the cylinder (approximately 0.24 m upstream and 0.61 m downstream). Calibration was typically carried out at 32 Hz and measurements during the tests at 200 Hz (the same than the velocity measurements).

An acoustic Doppler velocitymeter (ADV) Nortek Vectrino was used to record the three components of the flow velocity at a point in the vicinity of the cylinder. Velocity profiles were recorded upstream and downstream of the cylinder when the scour depth in the scour hole was deemed to be in equilibrium. The Vectrino does point measurements of the three components of flow velocity, and hence a system to move the ADV vertically with accuracy (approximately of 0.0003 m) was in place. Depending on the water depth there were 15 or 20 point measurements in the vertical from as close to the bed as possible. The ADV head is 0.0116 m in diameter. Therefore the measurement volume will be roughly 0.0058 m from the bed.
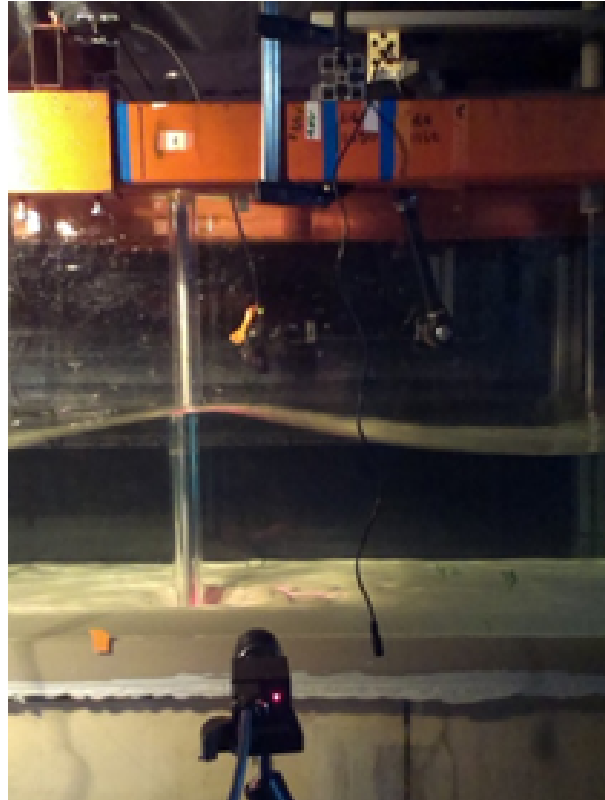
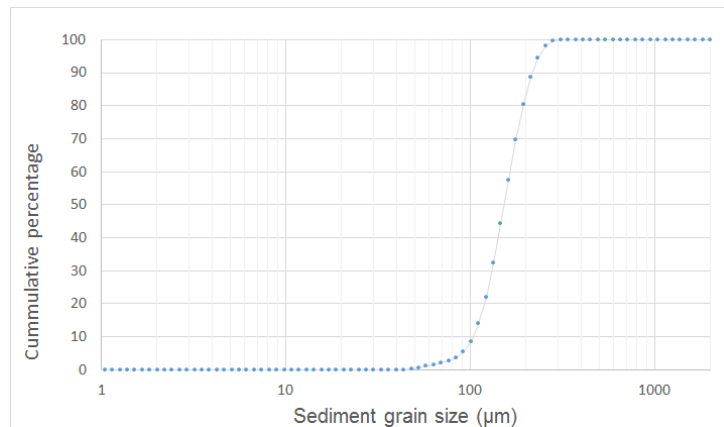Figure III.2: Set up at the flume

Figure III.3: Particle size distribution for laboratory sediment

Two methods of data acquisition were used during the tests: Synchronised (analogue) measurements of the free surface and flow velocity; and quasi-synchronised (digital) measurements, manually started both wave probes and ADV acquisition software virtually at the same time. Both systems recorded at 200 Hz the free surface and the flow velocity.

During the velocity profile measurement, the devices measured during 5 to 6 minute intervals (in order to have about 300 waves in the series). It is evident that some changes took place on the bed during the interval of velocity measurements. These changes in morphology are assumed to be small and the effect of those changes on the velocity, because there may be some, are assumed to be small. These changes in morphology may affect more the measurements nearer the bed.

Measurement of velocity profiles after 8 hr or more - when the scour depth at the scour hole is assumed to reach an equilibrium with the conditions. Measurement of velocity profiles were taken upstream and downstream of the cylinder (Figure III.4).
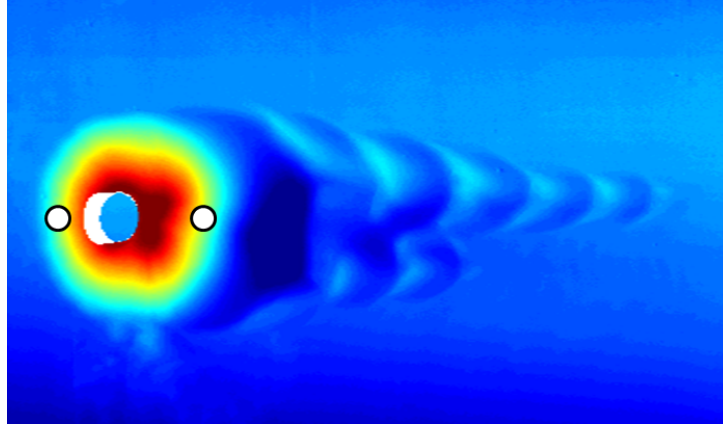
(a) Plan
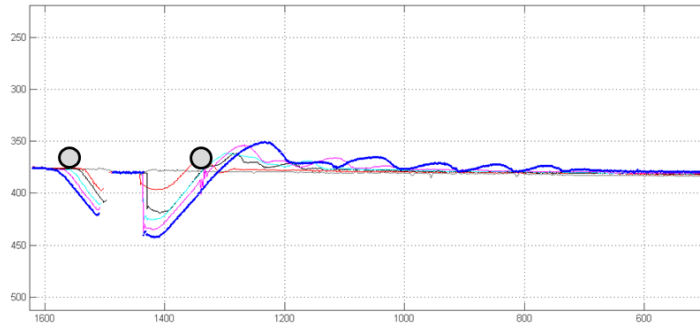
(b) Elevation

Figure III.4: location of velocity measurements end of tests

III.2.3.1 Visualisation, videos B/W and colour

A number of images, and videos were acquired during the length of the tests by a high speed acquisition camera (in B/W) aided by a diode laser plane to illuminate the flume and also by a compact digital camera.

III.2.3.2 Bed profile acquisition methodology

The bed profile acquisition system was adapted from **(author?)** [4] and consisted of a rail covering a distance within the flume of 1.22 m, a laser diode and high speed acquisition camera. The laser diode was looking down and the laser plane was perpendicular to the bottom of the flume. The laser diode and the camera were fixed to a frame that moved along the rail (III.5). The frame travelled over the rail moved by a step motor that was controlled by a PC. The angle between the camera and the bed as measured was $47.7°$, the angle between the camera and the laser plane was estimated as $42.3°$. The error of these measurements was estimated to be $0.3°$. The distance between the camera and the flume floor (how high it was placed above the bed) was a compromise between the angle of the features to be observed, the distortion of the image (also due to the water depth) and the width of the field amongst others. The bed profile acquisition system had 2 modes. Step mode and continuous mode. 1) The continuous mode: the frames with the camera and laser moved continuously as images are captured continuously, using a user interface to capture both at the same time. This system captured typically 2395 images; and 2) The step mode: the frame with camera and laser moved using said user interface to move the frame a prescribed number of steps, paused for a prescribed period and captured an image, then started again. This system captured typically 1620 images. This allowed the capturing of a finite number of images at a user defined spatial interval and with a defined pause between moving and image capture. The set up for the computer controlled step motor was:

- STEP system: 1620 images, 5 steps, 800 milliseconds pause.

- CONTINUOUS system: 2395, continuous, 8100 steps.

The captured image dimensions were 1024 x 768 pixels. Where there were 1024 pixels along the width of the flume x 768 pixels in the vertical. This acquisition system required post processing to digitise the information from the images.

III.3 Test conditions

To characterise the flow around a cylinder due to combined waves and currents and its effect on the bed a number of tests were carried out.

A number of initial experiments were carried out to characterise the hydrodynamics of the flume in the absence of the cylinder, measuring vertical velocity profiles over a fixed bed for water depths of 0.25 and 0.3 m for currents and waves only, and waves and currents.

Three complete mobile bed experiments were carried out to study the evolution of scour around a cylinder, with conditions shown in Table III.1.

Test No.	Wave height (m)	Wave period (s)	Wave frequency (Hz)	Current	Mean current speed (m/s)	Scale
Courseulles-sur-mer Storm conditions Tr = 1:10 yr	0.05	0.8	1.25	y	0.16	1:100
Current only	N/A	N/A	N/A	y	0.16	1:100
Synchronisation conditions	0.02	0.67	1.5	y	0.16	1:100

Table III.1: Test conditions for mobile bed cases, wave parameters shown without scale factor

III.4 Experimental procedure

The procedure during the test typically consisted of the following steps. The flume was filled up to the correct water depth, typically 0.3 m (0.25 m above the mobile bed). The instruments were calibrated, whether there were 2 or three wave probes. Due to the set up the wave probes could only be moved up, not down into the flume. Therefore typically the measurements corresponded to the free surface i.e. 0 m, then raised to 0.025, 0.05 and 0.075 m.

If the test involved mobile bed, this was screeded using the two bars placed along the bottom of the flume (that raised from the glass bed 0.05 m) to level the bed at a uniform level of 0.05 m. The bed was then swept by the profiling system, both in step-by-step and continuous mode.

The ADV vas placed downstream from the cylinder, the measurement volume placed along the centreline at approximately mid depth. The pump system was started manually to reach the required rpm (350) then then the paddle was started at the required amplitude and frequency.

After the required interval then waves were stopped and then the pump system. The cylinder was removed along with the ADV and the sweep for the acquisition of the bed profile was taken.
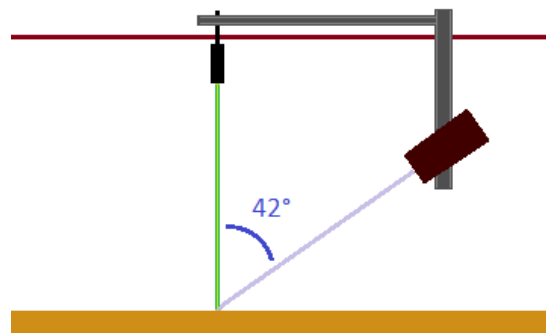

Figure III.5: camera-laser set up

III.5   Data analysis

III.5.1   Velocity and free surface

The velocity measurements collected by means of the ADV provide the three component of velocity at the point of measurement. These signals can at times be very nosisy especially true when measuring near the bed or another surface or when seeding particles are scarce. Various authors have developed toolboxes to clean the datasets without removing the turbulent components [2], [5], [7]. The analysis of the ADV data required post processing methods such as despiking toolbox, fast Fourier transform and filtering.

III.5.2   Post-processing of bed profile data

Each image contains a black background and white line that is the view of the bed at a given cross section transect of the flume. The contour is digitized by converting the image from RGB to gray scale and searching for the position of intensity higher than a threshold and calculating the mean of the position. The image is distorted (pincushion) more on the sides and less towards the center, this depends on the lens used. It can be corrected by subtracting the images from the initial bed profile to the subsequent profiles as distortion is assumed to be equal for the same position.

III.6   Results

Samples of the data collated during the experiments are shown in this section.

III.6.1   Velocity profiles and measurements

Velocity profiles with currents only over a fixed bed with water depth of 0.25 m, the pump set at 350 rpm or 450 rpm respectively in Figures III.6a and III.6b. Figure III.6c shows velocity profiles with regular waves only over a fixed bed with a water depth of 0.25 m and wave height (H) approximately 0.05 m and wave period (T) of 0.8 s.

III.6.2   Bed profiles

Profiles as collected by the acquisition system are shown for Test 1, with Courseulles-sur-mer conditions in Figures III.7 and III.8. Figure III.7 shows the top view and Figure III.8 shows the side view of the evolution of the scour hole and ripples behind the cylinder.

III.6.3   Scour depth plot

Scour depth values for Test 1 and 3 (Courseulles and Synchronisation condition respectively) were obtained by direct measurement to the side of the cylinder. These are plotted in Figure III.9, in log scale to show the evolution of the scour depth within the scour hole with time. The scour depth increases up to about 6 hr and then it starts to plateau for both cases. Further analysis of the bed profile data will yield more information regarding the changes in shape of the scour hole, and location of largest scour depth.

III.6.4   Visualisation images

Samples of black and white stills are shown in Figures III.10a and III.10b. A sample of colour image showing the visualisation with red laser is shown in Figure III.11. Full analysis of visualisation images may provide qualitative evidence on differences in flow behaviour around the cylinder as the scour hole evolves.
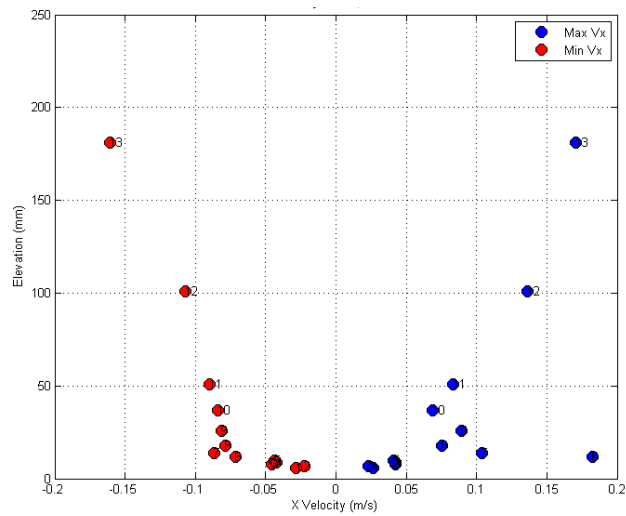
III.7   Summary

- A detailed dataset was collated in wave and current flume to characterise bed and hydrodynamic changes around a cylinder;

- High detailed bed profiles were recorded at regular time intervals for three test cases;
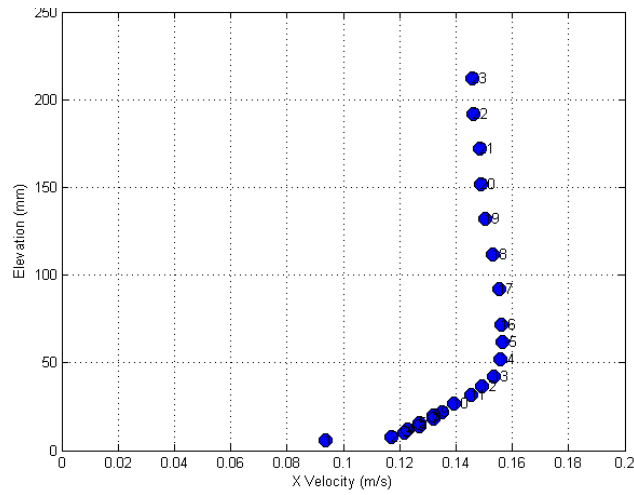
(a) Current only, 350 rpm
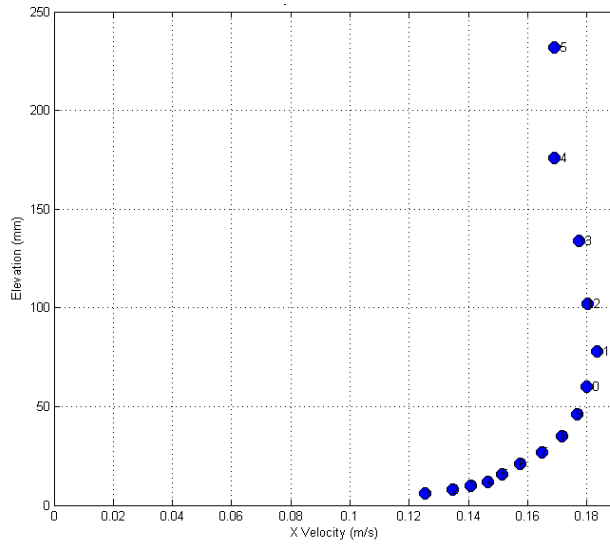
(b) Current only, 450 rpm

(c) Waves only, $H = 0.05$ m, $T = 0.8$ s. Blue and red markers indicate maximum and minimum velocities, respectively.
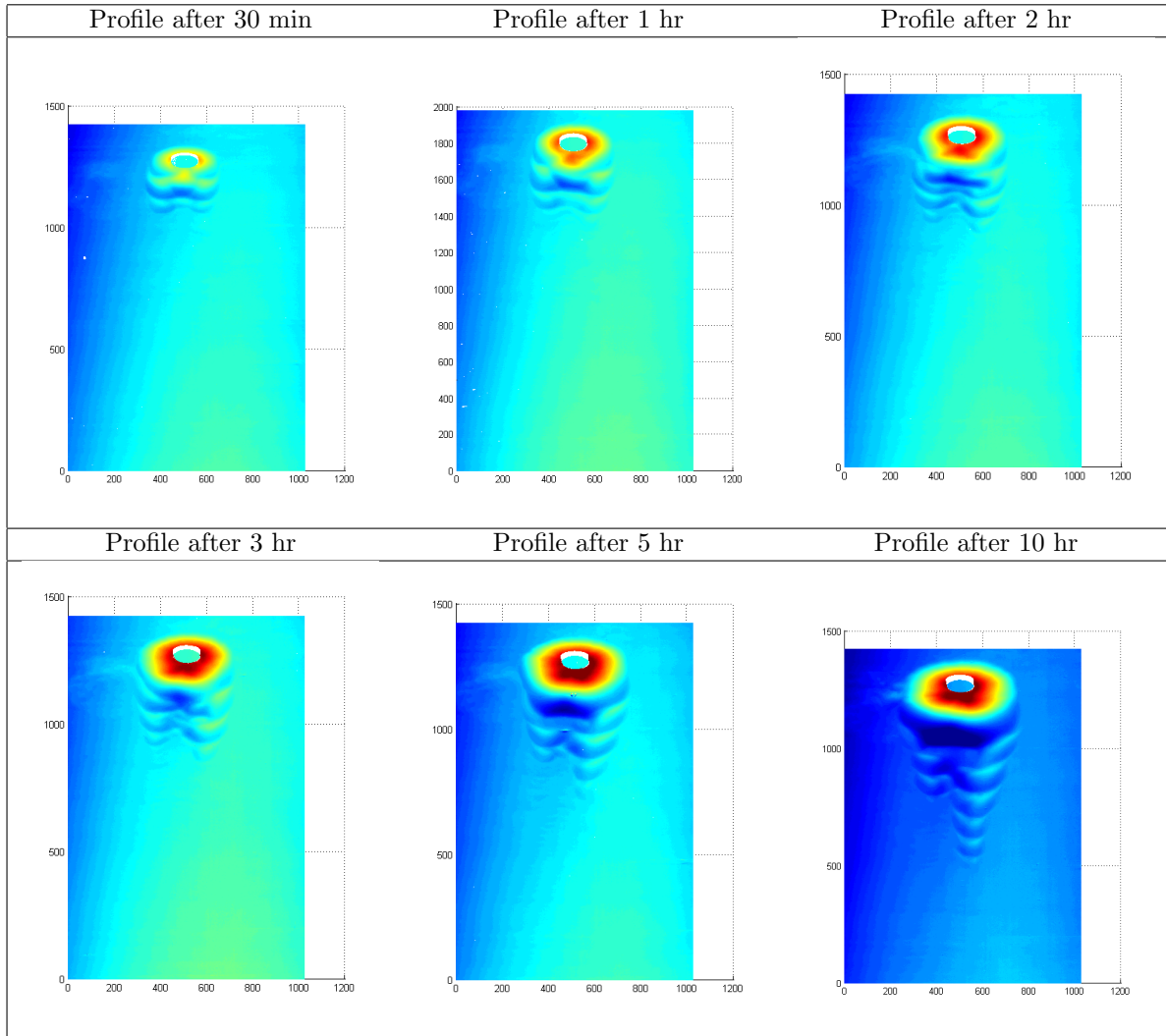
Figure III.6: Vertical velocity profiles.

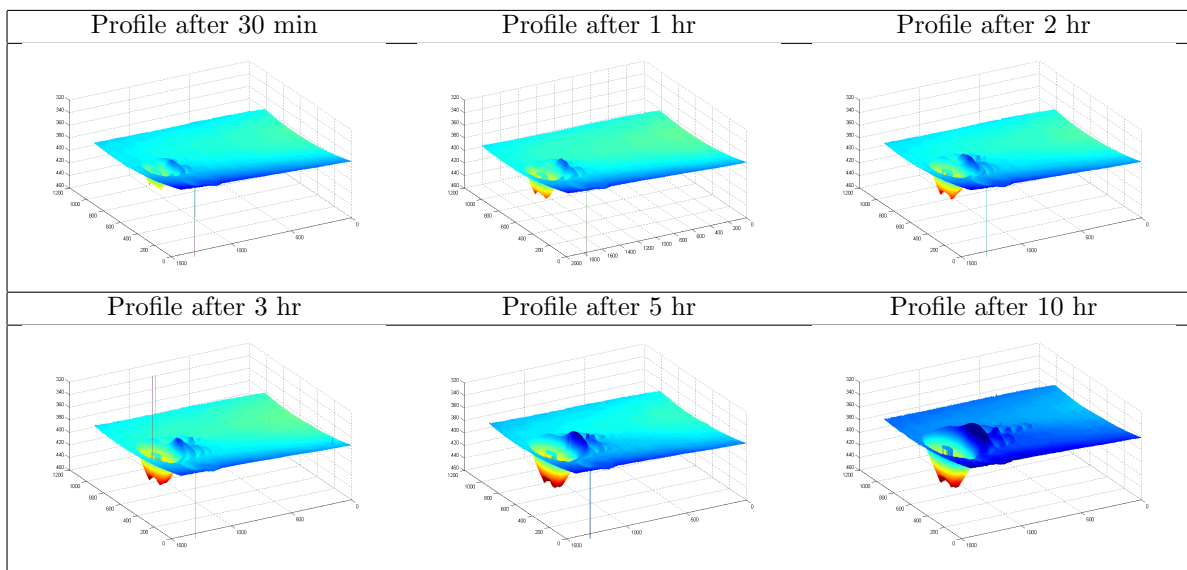Figure III.7: Bed profiles for Test 1 - with Courseulles-sur-mer. At t = 0.5, 1, 2, 3, 5 and 10 hr

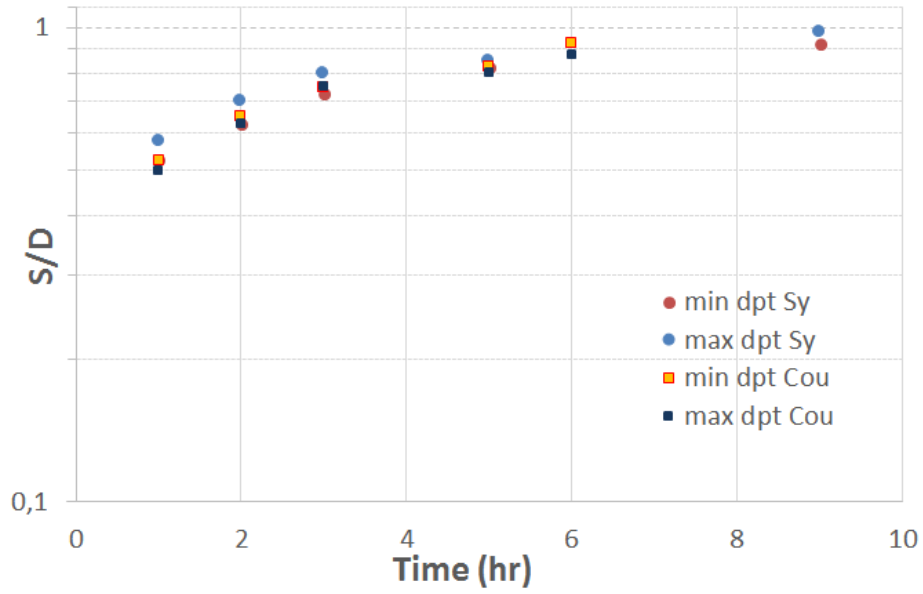Figure III.8: Bed profiles for Test 1 - with conditions from Courseulles-sur-mer. At t = 0.5, 1, 2, 3, 5 and 10 hr

Figure III.9: Variation of non-dimensional scour depth (S/D) with time
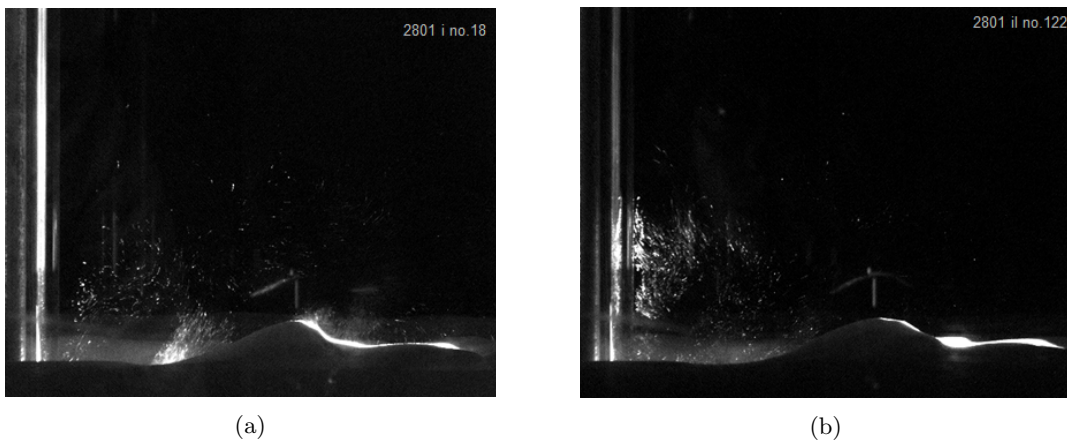

(a)

(b)

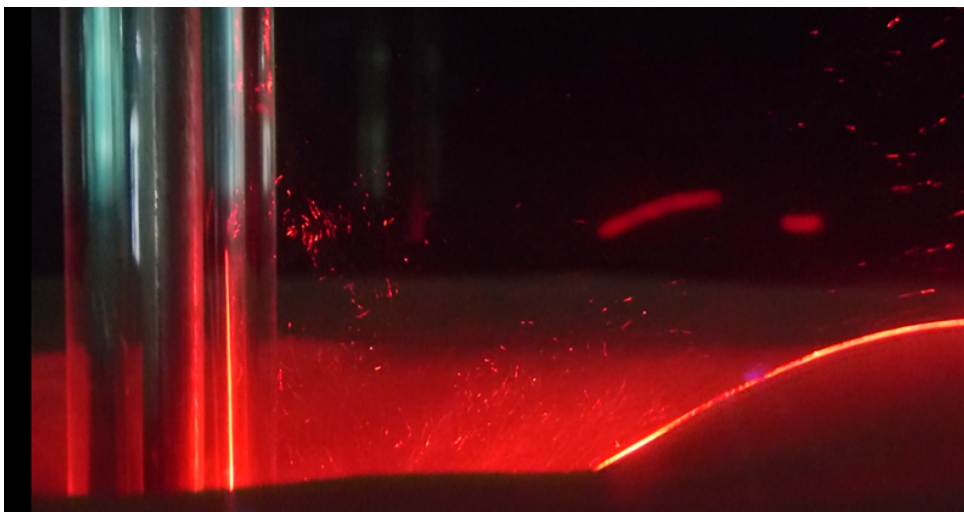Figure III.10: Black and white images of particle movement in the vicinity of the cylinder

Figure III.11: Image of particle movement in the vicinity of the cylinder

15

- Vertical velocity profiles were acquired upstream and downstream of the cylinder near the edges of the scour hole;

- Colour and black and white images recorded during the experiments that provide qualitative information on the evolution of the hydrodynamics around the cylinder and extent of field of influence of the cylinder;

- The regime during the experiments was clear-water scour, where the threshold of sediment motion is not exceeded except in the vicinity of the cylinder ($\theta > \theta_{cr}$);

- From black and white visualisation images it was observed that the height of bursts of suspension of sediment right behind the cylinder was up to half of the water depth;

- The effect of the cylinder on the bed downstream extended beyond $10 * D$.

III.8   Future work

- Analysis is on-going;

- Post processing of bed profile data;

- Estimate of turbulent kinetic energy and bed shear stress from velocity profiles (current only, wave only and combined waves and currents);

- Comparison with other experiments/data sets from OFELIA project.

III.9   Acknowledgments

References

[1] B Dargahi. The turbulent flow field around a circular cylinder. *Experiments in Fluids*, 12:1–12, 1989.

[2] Derek G Goring and Vladimir I Nikora. Despiking acoustic doppler velocimeter data. *Journal of Hydraulic Engineering*, 128(1):117–126, 2002.

[3] Peder Hjorth. *Studies on the nature of local scour*. Inst. för Teknisk Vattenresurslära, Lunds Tekniska Högskola, Lunds Univ., 1975.

[4] Julie Lebunetel-Levaslot. Dynamique de formation des reseaux de rides de sable en canal a houle.

[5] Bruce MacVicar, Scott Dilling, and Jay Lacey. Multi-instrument turbulence toolbox (mitt): Open-source matlab algorithms for the analysis of high-frequency flow velocity time series datasets. *Computers & Geosciences*, 73:88–98, 2014.

[6] Etienne PD Mansard and ER Funke. The measurement of incident and reflected spectra using a least squares method. *Coastal Engineering Proceedings*, 1(17), 1980.

[7] V.I. Nikora and D.G. Goring. ADV measurements of turbulence: Can we improve their interpretation? *Journal of hydraulic engineering*, 124(6):630–634, 1998.

[8] Andreas Roulund, B. Mutlu Sumer, Jrgen Fredse, and Jess Michelsen. Numerical and experimental investigation of flow and scour around a circular pile. *Journal of Fluid Mechanics*, 534:351–401, 2005.

[9] BM Sumer, N Christiansen, and J Fredsøe. The horseshoe vortex and vortex shedding around a vertical wall-mounted cylinder exposed to waves. *Journal of Fluid Mechanics*, 332:41–70, 1997.

[10] BM Sumer and J Fredsøe. Scour around pile in combined waves and current. *Journal of Hydraulic Engineering*, 127(5), 2001.

[11] Ulrich CE Zanke, Tai-Wen Hsu, Aron Roland, Oscar Link, and Reda Diab. Equilibrium scour depths around piles in noncohesive sediments under currents and waves. *Coastal Engineering*, 58(10):986–991, 2011.

IV

Laboratory modelling of resonant wave-current interaction in the vicinity of wind farm masts

H. Gunnoo, N. Abcha, A. Ezersky

IV.1   Introduction

In the nearest future, by 2020, about 4% of electricity in Europe will be supplied by sea stations operating from renewable sources: ocean thermal energy, wave and tidal energy, wind farms. By now the wind stations located in the coastal zone, provide the most part of electricity in different European countries. Meanwhile, effects of wind farms on the environment are not sufficiently studied. In order to improve our understanding of the environmental impacts of offshore wind farm foundations, laboratory simulation of the hydrodynamic fields has been performed. We report results of laboratory simulations aimed at investigation of hydrodynamic fields arising in the vicinity of wind farm masts under the action of currents and surface waves. The main attention is paid to modelling the resonance effects when the amplitude of velocity variations show significant growth in the vicinity of the masts under the joint action of currents and harmonic waves. This resonance can lead to an increase in Reynolds stress on the bottom, intensification of sediment transport and sound generation.

IV.2   Experimental set-up

The experimental study is conducted in the wave flume of the Laboratory of Continental and Coastal Morphodynamics, in Caen. This flume (Figure 1) has a length of 18 m, a width of 0.5 m, while water depth can vary from 0 to 0.4 m. Waves of different frequency and amplitudes are generated in the flume under conditions of deep water and shallow water. To generate surface waves in the flume, a computer controlled wave maker is used.

Experimental facilities allow us to investigate propagation of surface wave with in combination with an opposing steady current. This current is generated by means of a pump, as indicated on Figure 1. In order to reduce the intensity of turbulent fluctuations created by the pump, two honeycombs with a thickness of about 10 cm each are installed in the channel, as shown in Figure 1, down-wave from the cylinder.To study the evolution of free surface displacement along the channel resistive probes are used. The characteristics of the hydrodynamic fields are measured thanks to Acoustic Doppler velocimetry (ADV). This measuring device is placed at a distance of several diameters down-stream from the cylinder and measures the three components of velocity: V_x (transverse velocity), V_y (longitudinal velocity), V_z (vertical velocity) as shown in Figure IV.1.

IV.3   Sub-harmonic frequency lock-in

The study of sub-harmonic frequency lock-in for the vortex wake of a cylinder was conducted in two series of experiments, for a wave of frequency f and Reynolds numbers between $Re = 6 * 10^3$ and 10^4. Sub-harmonic frequency lock-in is manifested in the fact that a periodic or quasi-periodic oscillation with
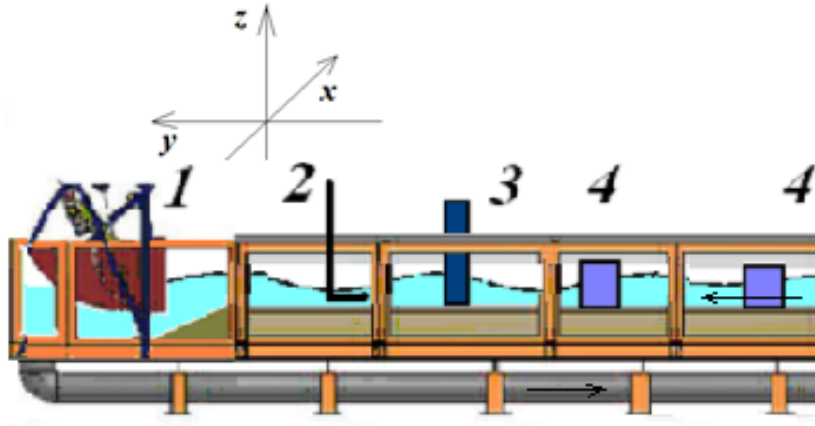
Figure IV.1: Experimental sketch: 1 refers to the wave maker, 2 refers to the ADV, 3 refers to the location of the cylinder, 4 is for the honeycombs; arrows indicate directions of current.

half the frequency of the wave ($f/2$) appears in the wake of a cylinder under the action of surface waves with a frequency f. The lock-in takes place when the wave frequency is reasonably close to half the shedding frequency. In general this frequency coincides with the Strouhal frequency (f_{Sh}). It should be noted that the surface waves generated computer-controlled wave maker has a very narrow frequency spectrum.

Effect of surface waves on a vortex street led to the appearance of oscillations in the wake with a peak at half the frequency ($f/2$) and the finite width of the spectral peak. Only when a sufficiently large amplitude of the surface wave is excited, the spectrum of velocity fluctuations shows a narrow frequency peak at a half frequency ($f/2$). It is therefore necessary to choose a criteria by which one could determine if the frequency lock-in occurs or not. As such criteria, we chose the width of the spectral peak: if the width of the spectral peak at the level of 10 dB is less than 3%, the mode is classified as a mode of seizure frequency. If the spectral component with frequency ($f/2$) is clearly visible, but the width of the peak is more than 3 percent, such a regime is defined as partial lock-in.

To construct diagrams, Fourier spectra of velocity fluctuations V_x were used. This component of the velocity determined mainly the hydrodynamic mode, namely the vortex behind the cylinder. Results for the $Re = 10^4$ regime are shown in Figures IV.2 and IV.3.

IV.4 Visualisation of velocity fields

In order to understand what the spatial structure that arises in the cylinder wake when the amplitude of the surface waves increases, flow visualization and measurements of velocity fields by particle tracking velocimetry (PTV) method were carried out for different regimes at Reynolds number $Re = 10^4$. In the absence of surface waves, the Karman Vortex street is irregular in space and vortex shedding does not occur periodically in time. Example of a snapshot of the particle concentration and velocity field is shown in Figure IV.4. The cylinder is show in grey colour. This regime corresponds to the spectrum shown in Figure IV.3a.

The action of surface waves leads to lock-in of shedding frequency. Results of surface wave action depend on wave amplitude. For small amplitude sub-harmonic frequency lock-in occurs. Figure IV.5 shows a snapshot that corresponds to the velocity spectrum presented in Figure IV.3c. Spectrum of velocity fluctuations in this case has a pronounced peak at a frequency equal to half the frequency of the surface wave. It should be noted that the spatial structure of the Karman street does not display any qualitative changes in comparison to the previous case (see Figures IV.4 and IV.5). The Karman street has chess like vortex structure.

The qualitative changes in spatial structure of the Karman street are observed for larger wave amplitude: instead of the chess like vortex structure, alternating chess-like and symmetric vortex shedding
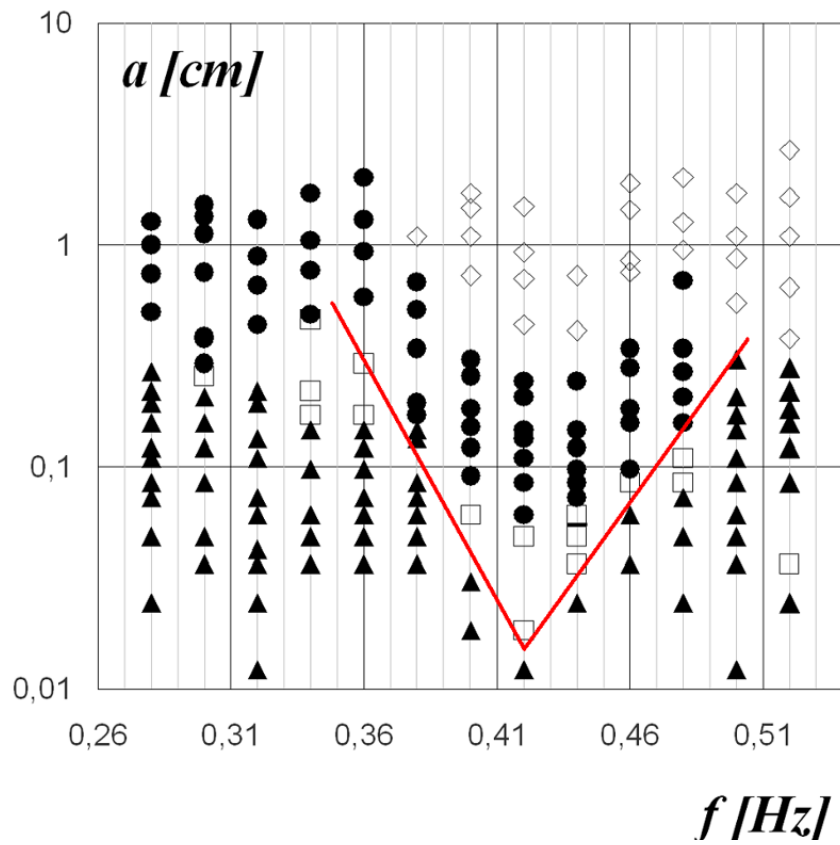
Figure IV.2: Parameter plane showing the amplitude of the surface wave vs wave frequency. Four regions with qualitatively different dynamics of vortices in Karman street are found: absence of sub harmonic frequency lock-in (▲), partial sub harmonic frequency lock-in (□), sub harmonic frequency lock-in (•) and harmonic frequency lock-in (◊). The red line delimits the regions corresponding to sub-harmonic frequency lock-in the vicinity of $2f_{Sh}$
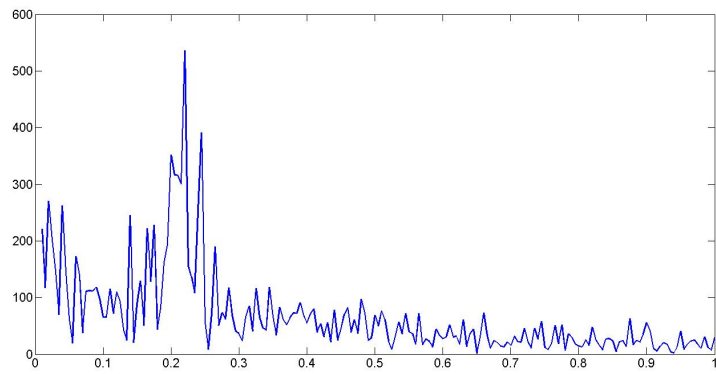
(a) Absence of sub-harmonic frequency lock-in.
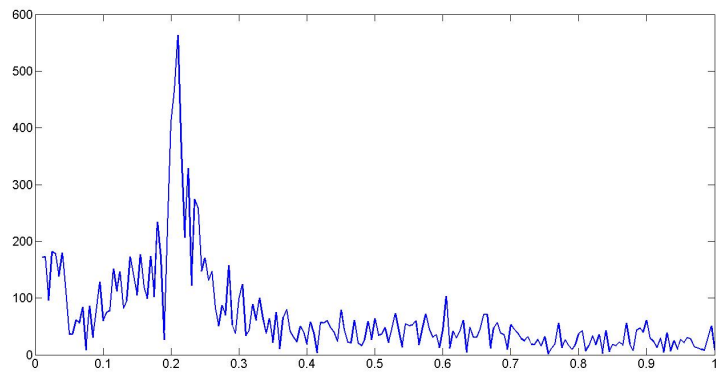
(b) Partial sub-harmonic frequency lock-in.
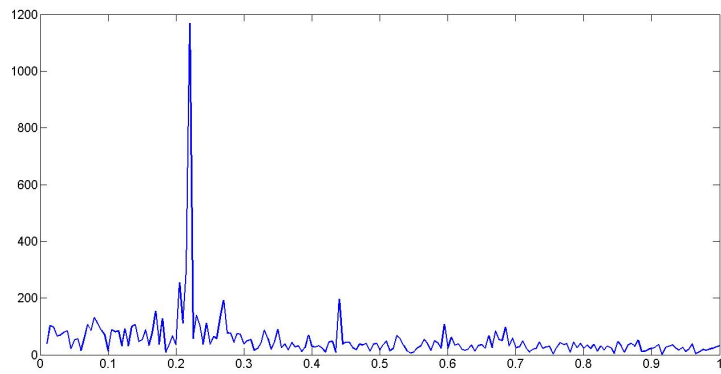
(c) Complete sub-harmonic frequency lock-in.
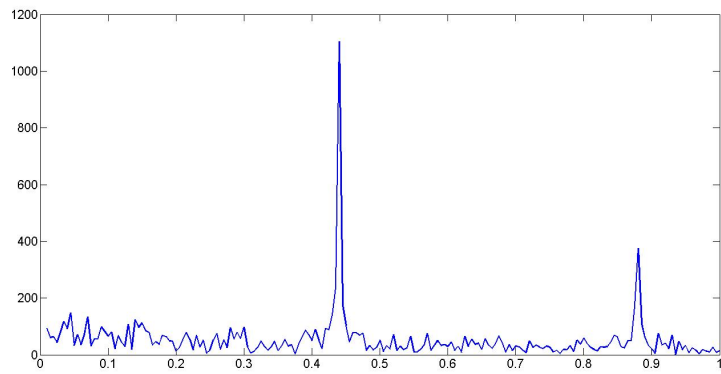
(d) Harmonic lock-in.

Figure IV.3: Examples of spectral plots of the along flume horizontal velocity component (V_x).

Figure IV.4: Example of flow visualization and field of velocity obtained by PTV, amplitude of surface wave $a = 0$ (current only)

Figure IV.5: Example of flow visualization and champ of velocity obtained by PTV, amplitude of surface wave $a = 0.3cm$, $f = 0.45Hz$

Figure IV.6: Example of flow visualization and champ of velocity obtained by PTV , amplitude of surface wave $a = 0.8cm$, $f = 0.45Hz$

occurs. With further increase of wave amplitude alternating symmetric and antisymmetric vortex shedding occurs. When a sufficiently large amplitude waves ar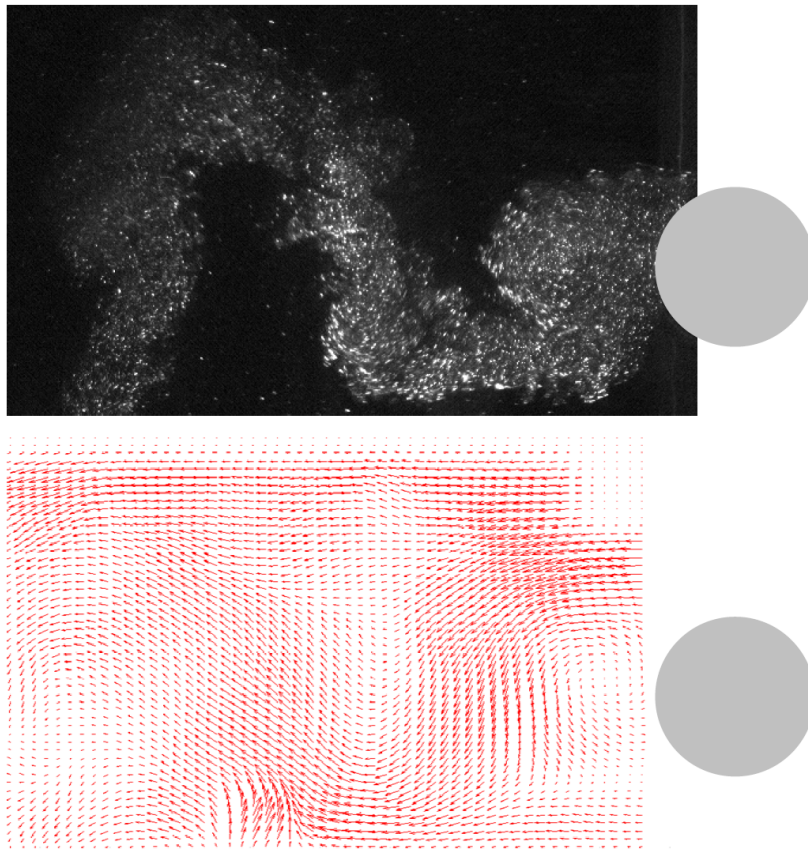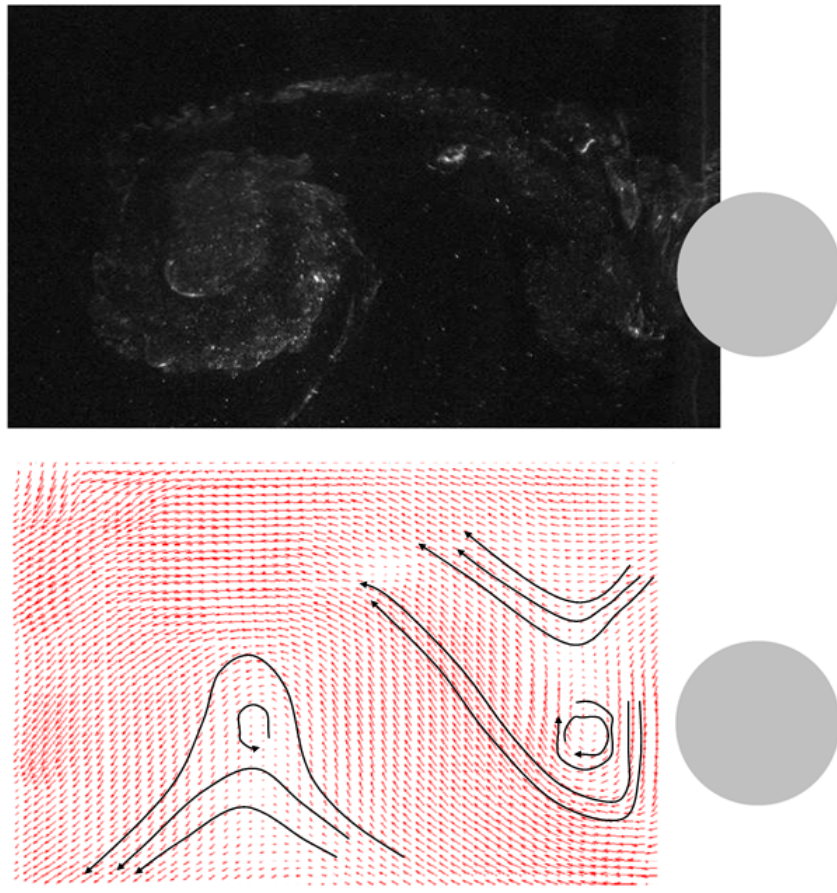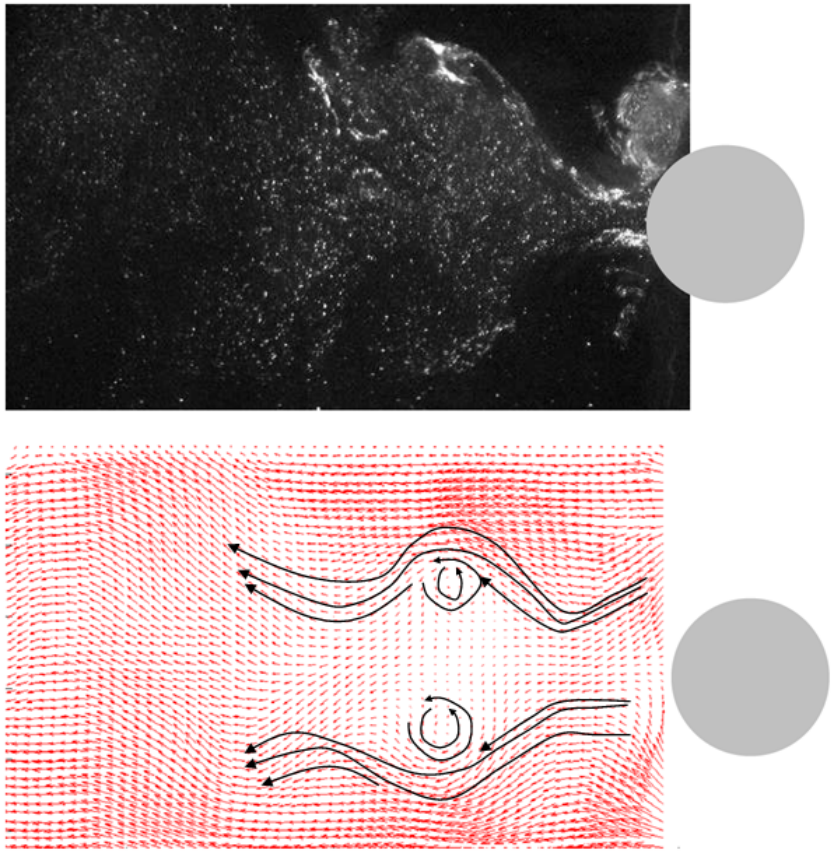e applied, a transition to a symmetric vortex shedding occurs. This mode appears as result of the increasing duration of the symmetric phase with increasing of wave amplitude. Example of flow visualization and velocity field of such regime is shown in Figure IV.6. Velocity fluctuation spectrum contains harmonic at frequency $2f$, where f is the frequency of the surface wave (see Figure IV.3d). For large amplitudes vortex shedding is suppressed and neither symmetric vortex nor chess like Vortex street appear behind the cylinder.

IV.5   Discussion of results

In this summary it has been shown that surface waves can change both the spectrum and intensity of the velocity fluctuations in the wake of a cylinder. It was observed that during a state of sub-harmonic frequency lock-in, the root mean square fluctuations of velocity in the Karman street may be doubled. Results demonstrated in this report were obtained for Reynolds number of the order of $Re = 10^4$. The same order of amplification for fluctuations of velocity have been found for lower Reynolds number $Re = 6.4 \times 10^3$. Such an increase occurs for surface waves with moderate amplitudes. Further increasing of the surface wave amplitudes lead to suppression of vortex shedding and essential decreasing of root mean square velocity fluctuations in the vortices behind cylinder.

IV.6   Conclusions

1. Frequency lock-in of vortex shedding behind obstacle in water flow is observed under the influence of surface wave with small amplitudes.

2. For stream-wise wave propagation, the sub-harmonic frequency lock-in in a chess-like Karman vortex street occurs when wave frequency is two times more than the frequency of shedding.

3. There exists interval of surface wave amplitudes for which sub-harmonic frequency lock-in occurs. For small amplitudes the absence of sub-harmonic frequency lock-in is due to the influence of turbulence. For large amplitudes, instead of chess-like Karman street, symmetric vortex street is excited; such vortex street is unstable.

V

Hydrodynamics study of waves-monopile interactions next to the seabed for strong events

J. Lebunetel, I. Garcia-Hermosa, G. Perret, J. Brossard

V.1 Introduction

In the last ten years the requirements to generate energy from cleaner sources have pushed the renewable energy industry. Deadlines like the 2020 UK target to achieve the 15% of the national energydemand from renewable sources [3] resulted in the rapid expansion of the offshore wind energy (33-58 Twh by 2020). The 3rd Round of proposed offshore wind farm sites in the UK were awarded in 2010 and in France the second call for proposals was awarded May 2014 and a third is expected soon. The French governments goal by 2020 for renewable energy is 23%, including 6000 MW of installed marine energy capacity [1]. Moreover, Frances offshore wind potential is 90 TWh. These latest proposed developments are being pushed to deeper waters and have increased in scale and technical complexity with ever growing mast diameters and varying foundation options. The choice of mast foundation depends on factors such as: soil characteristics, water depth, hydrodynamic conditions and costs. These factors highlight the need to understand further the local and regional impacts of wind farm foundations. There have been numerous studies dating from the eighties and nineties investigating the effect of a cylinder on regular wave dynamics [2, 11]. The flow structures developing near the bed due to the presence of a cylinder may be responsible for scour around the structure. Horseshoe vortices are flow structures associated to scour processes at the upstream end of a cylinder [11, 12]. According to existing literature [15] the Keulegan Carpenter (KC) number ought to be larger than 6 in order for horseshoe vortices to be present.

$$KC = \frac{U_m T}{D} \tag{V.1}$$

where U_m is the bottom orbital velocity, T wave period and D the cylinder diameter. In fact, Sumer et al. **(author?)** [11] observed that typically the horseshoe vortex is suppressed for $KC < 6$. They also showed that vortex shedding was present for $KC > 4$. More recent studies characterized the different vortex modes on vertical planes along the cylinder [14] and in horizontal planes [10, 7]. Those studies have been conducted for regular waves. The present investigation aims to widen the knowledge base by providing qualitative and quantitative data in the vicinity of the cylinder to understand the effect of the presence of the cylinder on the bed for irregular waves and a KC number smaller than 4. Local physical processes are investigated experimentally.

V.2 Experimental set-up

V.2.1 Facilities

The wave flume located in LOMC is 35 m long, 0.90 m wide and 1.2 m in height (Figure VII.1). These dimensions enables to performed experiments at scale 1 : 60 and 1 : 40. A wave generator was located at

the offshore end, and a spending beach at the inshore end of the flume. The paddle was controlled by a computer system where long crested regular wave conditions were generated by inputting wave height and period. Irregular waves were generated by inputting the significant wave height and peak period assuming a JONSWAP spectrum. The duration of the tests was either 300 wave cycles for regular waves or a full spectral cycle for random waves. The diameter of the monopile foundation tested was 6 m at prototype scale leading to 0.10 m and 0.15 m at scale 1 : 60 and 1 : 40 respectively. For the purpose of the tests, the flume bottom was raised with a wooden false floor so that the floor was flushed with the side glass window to ease visualization/image capturing in the near-bed region. In the area of the cylinder the floor was a transparent Plexiglas board of 20 mm thickness to allow transmission of the laser beam and/or image capture. During all tests eight resistive wave gauges were placed along the flume grouped in two sets to aid analysis and to provide information on incident and reflected wave conditions [4]. An additional resistive wave gauge was placed in the close vicinity of the cylinder. The wave gauges were calibrated daily.
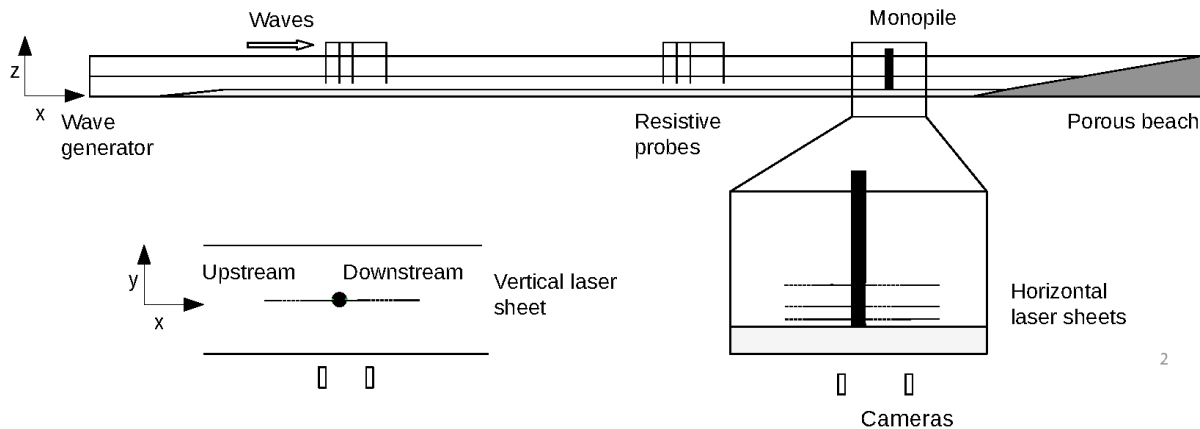

Figure V.1: Experimental setup: plan view showing longitudinal and transverse laser sheets for PIV measurements

V.2.2   ADV measurements

V.2.2.1   Set-up

The three components of flow velocity around the cylinder were measured with an acoustic Doppler velocimeter (ADV) at various positions and water depths in the vicinity of the cylinder. During the experiments the ADV was mounted on a moving frame which position could be changed through a computer interface or directly on the machine in the across- and along-flume directions with an accuracy of 0.1 mm. The three components of velocity were measured at up to 100 points (Figure V.2) at three depths above the bed (at $z/D = 0.11; 0.33; 0.61$) some measurements were repeated at a relative depth of 0.13 at the end of the course of experiments. Once the ADV was positioned at the desired measurement location, the free surface at the independent probe and flow velocity were recorded in a quasi-synchronised manner.

V.2.2.2   Test conditions

Using a 1 : 60 scale and Froude scaling criteria, the wave conditions correspond to a return period of 1 in 10 years at the Coureulles-sur-mer site. These are: significant wave height of 5 m, peak period of 8 s and water depth of 25 m and a cylinder of 6 m diameter. The ADV data required to be cleaned by using the method developed by Goring and Nikora [5] and modified by Mori et al. [8]. The free surface data needed to be re-synchronised with the velocity measurements due to a short time lag between the start of the free surface measurement and the ADV.
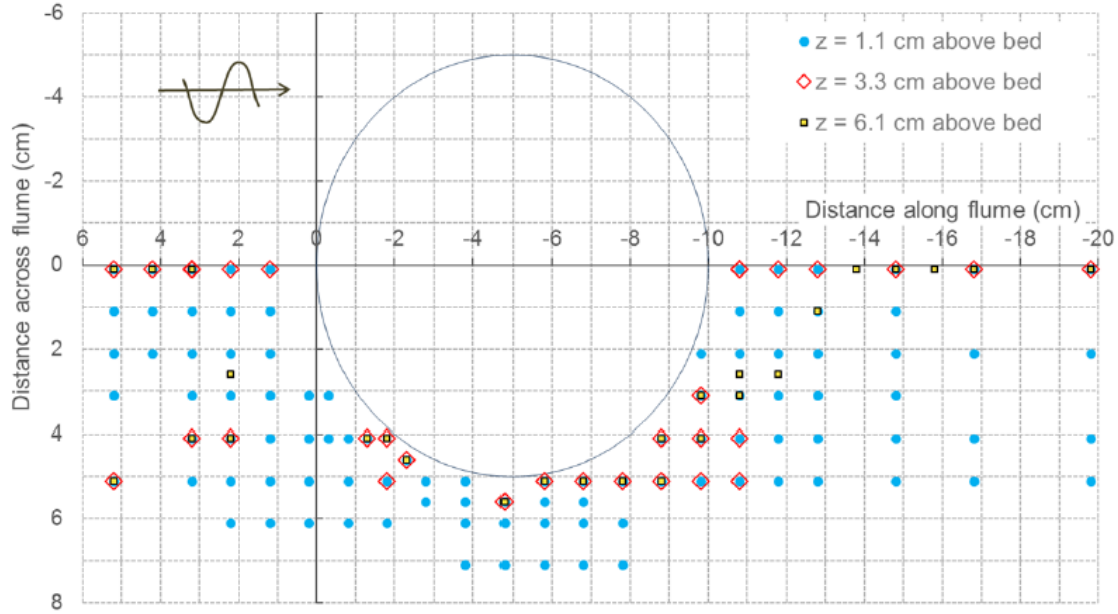
Figure V.2: Location of ADV measurements of flow velocity at three depths above the bed, showing the cylinder and the incoming wave direction

V.2.3 Particle Image Velocimetry

V.2.3.1 Measurement system

The PIV system included au double pulsed YAG laser (15Hz, 120mJ/pulse), a CCD camera at $30Hz$ and $1.9M$ pixels resolution, and R&D Vision softwares. The mean diameter of the seeding particles was of $50\mu m$. The time separation between two laser pulses was adjusted according to the flow velocities and equal to 15ms. The acquisition frequency of the velocity fields is 15Hz. The PIV system measurement was synchronised with the free surface probe. The high resolution camera was located at the side or beneath the flume, depending on the location of the laser light sheet. The velocity fields were thus measured in the vertical plane or the horizontal one at the streamwise and spanwise of the pile. For PIV measurements in the (x;z) plane, a vertical laser sheet was projected from the bottom of the channel through a transparnet bottom, across the centerline of the cylinder. The camera was then located at the side of the flume and capture images through a glass window. For PIV measurements in the (x;y) plane, the horizontal laser sheet was projected from the side of the channel through a glass window at a known distance from the bed z/D. The camera acquires pictures from the bottom of the flume through a glass window and the Plexiglas floor. Depending on the measurement window, the spatial resolution of the camera was within the following range : 0.03-0.21 mm/pixel. The calibration procedure and the PIV cross-correlation were performed with the DirectPIV software.

V.2.3.2 Post-processing

Before calculating the displacement vectors, a mean image was substracted to each image to improve contrast between the background and the particles. A mask was applied to blank out areas of the image that are of no interest. Then, the data processing followed three main stages of post-processing. These consists in convert from digital image to particle displacement, calibrate images to obtain velocity vectors and apply global, local and interpolation filters to remove spurious vectors. Flow velocity fields are thus obtained (Ux, Uz for the vertical plans, and Ux, Uy for the horizontal sheets). The vorticity fields were also obtained. Data were then analysed with Matlab at the prototype scale. Considering vertical PIV sheets, polynomial interpolation of the velocity fields have been performed to properly analyse the gradient of the velocity. Considering horizontal planes, streamlines have been calculated (Figure V.3) and the vorticity fields were available. The repetitivity of the wave spectrum and of the velocity measurements have been controlled (Figure V.4).
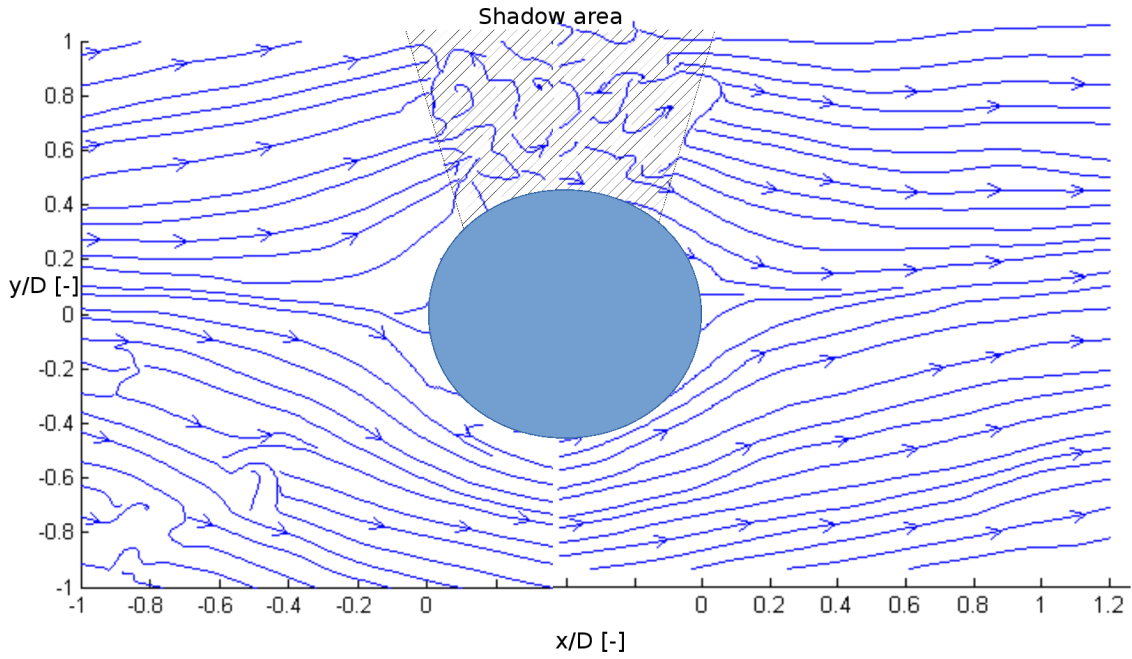
Figure V.3: Streamlines around the pile - H_s=5m ; T_p=8s
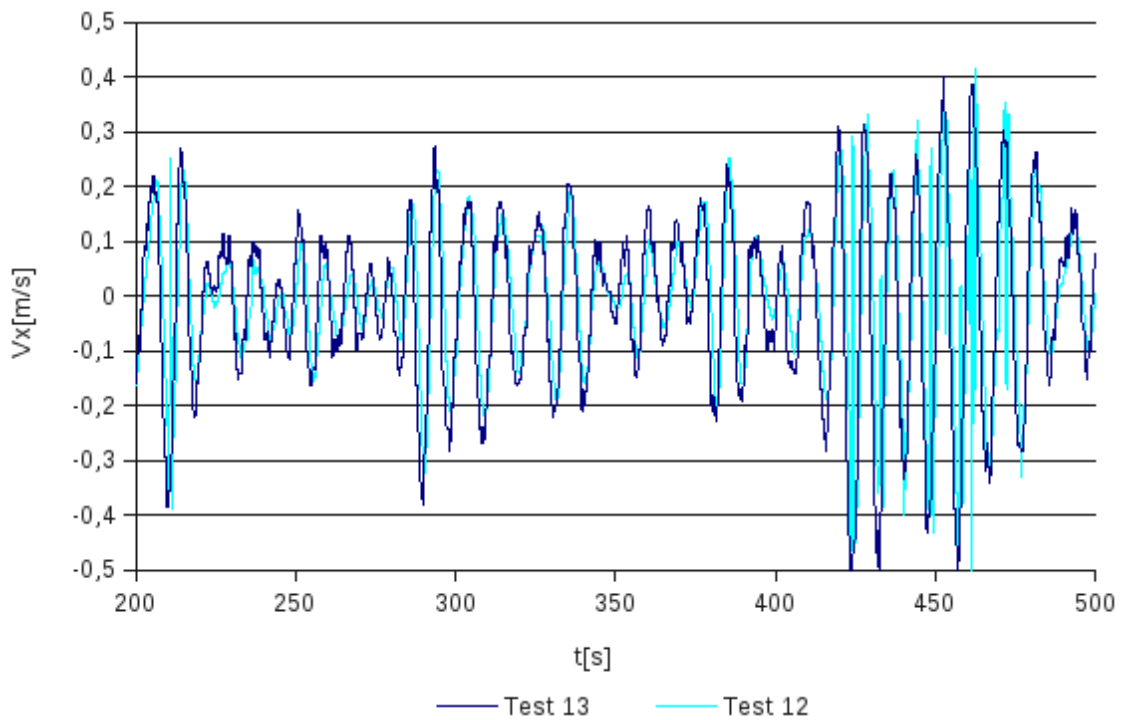
Figure V.4: Example of measured upstream velocities ($x/D = -0.14; z/D = 0.1$) for Test 12 and Test 13

V.2.3.3 Test conditions

A set of 29 experiments has been performed at scale 1 : 40 to characterize the flow around the cylinder due to wave action, in 2D planes for both regular and irregular waves. The experimental conditions are given in Table V.1.

The two components of the flow velocity were measured using PIV techniques (vertical sheet: x, z velocity components and horizontal sheet: x,y velocity components). Tests with the same flow conditions were performed considering several PIV sheets to characterize the flow all around the pile (Figure VII.1).

Table V.1: Experimental conditions

Test	Test class	Laser plane	View	Resol [mm/pix]	Waves IR/R	Scale	d [m]	T_p [s]	H_s [m]	R_e [-]	KC [-]
1	STORM	V	DS	LA	IR	40	25	8	5	$7.2\ 10^5$	1
2	STORM	V	DS	LA	IR	40	25	8	5	$7.2\ 10^5$	1
3	STORM	V	DS	LA	IR	40	25.04	8	5	$7.1\ 10^5$	1
4	STORM	V	DS	LA	IR	40	25.04	9	5	$11.9\ 10^5$	1.4
5	STORM	V	DS	LA	IR	40	25.02	10	3	$6.1\ 10^5$	1
6	STORM	V	DS	SZ	IR	40	25.02	9	5	$11.9\ 10^5$	1.4
7	STORM	V	DS	SZ	IR	40	25	8	5	$7.2\ 10^5$	1
8	KC	V	DS	0.15	R	28	10.59	12	5	$32.1\ 10^5$	2.6
9	KC	V	DS	0.15	R	28	10.57	12	5	$89.6\ 10^5$	4.3
10	KC	V	DS	-	IR	28	10.57	12	5	$89.6\ 10^5$	4.3
11	STORM	V	DS	0.03	IR	40	25.06	8	5	$7.1\ 10^5$	1
12	STORM	V	US	0.03	IR	40	25.04	8	5	$7.2\ 10^5$	1
13	STORM	V	US	0.14	IR	40	25.04	8	5	$7.2\ 10^5$	1
14	STORM	V	US	LA	IR	40	25.04	9	5	$11.9\ 10^5$	1.4
15	STORM	V	US	LA	IR	40	25.04	10	3	$6.1\ 10^5$	1.4
16	KC	V	US	0.14	R	28	10.63	12	3	$31.9\ 10^5$	2.6
17	KC	V	US	LA	R	28	10.63	12	5	$88.5\ 10^5$	4.3
18	KC	V	US	LA	IR	28	10.63	12	5	$88.5\ 10^5$	4.3
19	STORM	H-z/D=0.20	DS	0.11	IR	40	24.98	8	5	$7.2\ 10^5$	1
20	STORM	H-z/D=0.17	DS	-	IR	40	24.98	8	5	$7.2\ 10^5$	1
21	STORM	H-z/D=0.09	DS	0.20	IR	40	24.94	8	5	$7.2\ 10^5$	1
22	STORM	H-z/D=0.50	DS	0.22	IR	40	24.94	8	5	$7.2\ 10^5$	1
23	STORM	H-z/D=0.21	US	0.21	R	40	10.58	12	3	$32.2\ 10^5$	2.6
24	STORM	H-z/D=0.21	US	-	R	40	10.54	12	5	$90.2\ 10^5$	4.3
25	STORM	H-z/D=0.21	US	0.21	IR	40	24.94	8	5	$7.2\ 10^5$	1
26	STORM	H-z/D=0.09	US	0.20	IR	40	24.94	8	5	$7.2\ 10^5$	1
27	STORM	H-z/D=0.50	US	0.22	IR	40	24.94	8	5	$7.2\ 10^5$	1
28	STORM	H-z/D=0.50	SI	0.20	IR	40	24.94	8	5	$7.2\ 10^5$	1
29	STORM	H-z/D=0.09	SI	0.20	IR	40	24.94	8	5	$7.2\ 10^5$	1

For those tests, the flow conditions were the following: irregular waves with significant height of 5m, peak wave period of 8s (10 year return period for Courseulles site) and a water depth of 25m.

To properly analyze the results, evolution with time of the local flow characteristics is needed. Thus, each wave is isolated using a zero-up crossing criteria. Local wave height, period, wavelength and velocity are determined. The range of the local parameters of the flow (minimum, maximum and most probable values) are listed in Table V.2.

Table V.2: Range for flow conditions considering irregular waves (H_s=5m; T_p=8s)

Parameter	H [m]	T_p [s]	L [m]	U [m/s]	KC [-]	Re [-]	τ_{theo}
Range	1-9	5-13.5	44-190	0.05-1.36	0.04-1.99	$2.1\ 10^3$-2.4	0-1.4
Dominant value	3	8.5	100	0.5	0.8	$1.0\ 10^5$	0.2

In the following document, results focus on the tests performed with storm conditions (10 years return period event at the wind farm of Courseulles sur mer). The analysis of the results obtained with the KC tests are still in progress.

V.3   Results

V.3.1   3D velocities

A large number of ADV measurements points have been investigated in the vicinity of the pile to deeply examine the velocity characteristics in the three dimensions. As a first step, common experiments have been performed in the three facilities committed in the OFELIA project (LOMC of Le Havre University

and M2C of Caen University). The comparison of ADV results obtained in several facilities aims to ensure the validity of the reproductivity of the physical processes at different scales. Except for measurements performed very next to the bottom, where some devices faced issues to acquire noiseless signals, results are quite satisfying. Figure V.5 shows the comparison between velocity measurements in Le Havre and Caen experiments at $z/D = 0.33$ downstream the pile. The order of magnitude of velocities are similar and vx follows sinusodal shapes. Comparisons between horizontal velocities of ADV and PIV at the same location are actually in progress to assess the efficiency of the two measurement methods with similar acquisition frequency.
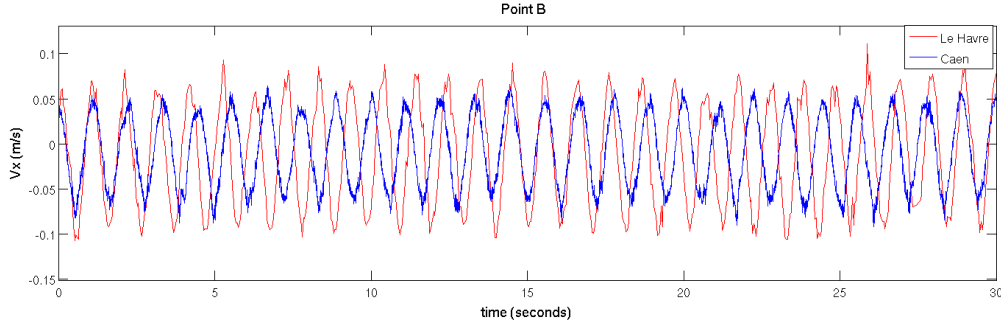

Figure V.5: Comparison between velocity measurements in Le Havre and Caen experiments

V.3.2 Velocity fields

V.3.2.1 Flow regime

The flow regime needs to be defined to properly analyse the following results. The velocity fields were measured in order to define the impact of the pile on the flow and on the generated stresses on the bottom. The bottom friction f_w depends on the flow regime and gives access to bottom shear stress data and thus to the capacity of the sediment to move and be transported. Considering that the experiments were performed with random waves, the flow regime might vary along the test. The flow conditions for each individual wave were reported in figure V.6. It depends on the ratio $\frac{a}{k_s}$, where a is the orbital excursion amplitude, and on the flow Reynolds number $R_e = \frac{a^2\omega}{\nu}$, where $\omega = 2\pi T$ is the wave pulsation, T is the wave period [s] and ν is the cinematic viscosity [m^2/s]. The bed roughness as been set considering common values for concrete bottom: k_s =0.001m (main bed material in the flume). The relatively weak roughness combined with the R_e values obtained, means that the experimental conditions belong to transitional to rough turbulent flow regime. The theoretical bottom shear stress $\tau_{theo} = 0.5\rho(a\omega)^2 f_w$ is evaluated as a function of the flow friction. Myraugh [9] introduced an implicit formulation for f_w, valid in both regimes.

$$\frac{0.32}{f_w} = \left(\ln\left(6.36\frac{a}{k_s}f_w^{0.5}\right) - \ln\left(1 - \exp\left(-0.0262\frac{R_e f_w^{0.5}}{\frac{a}{k_s}}\right)\right) + \frac{4.71\frac{a}{k_s}}{R_e f_w^{0.5}}\right)^2 + 1.64 \qquad (V.2)$$

V.3.2.2 Shear stress characterization

The scour phenomenon is strongly dependent on the bottom shear stress τ_b that can be estimated as a function of the velocity gradient $\tau = \frac{\partial u}{\partial z}\rho\nu$. From the PIV fields, this is the more accurate way to calculate the shear stress. The shear stress fields have been calculated considering the polynomial interpolation of the measured velocity to avoid non relevent velocities changes (Figure V.7). Bed shear stress can also be estimated as a function of the friction velocity $u^* = \sqrt{\tau_b\rho}$. But, the friction velocity is very tricky to obtain. The equation V.3 gives the expression of the velocty with z_0 depending on both the ruguosity k_s and the flow regime. Those methodologies need to be confronted for both measurment technics (PIV and ADV-vectrinos measurements performed within the experiments reported in Section VII).

$$u\left(z\right) = \frac{u^*}{\kappa}\ln\left(\frac{z}{z_0}\right) \qquad (V.3)$$
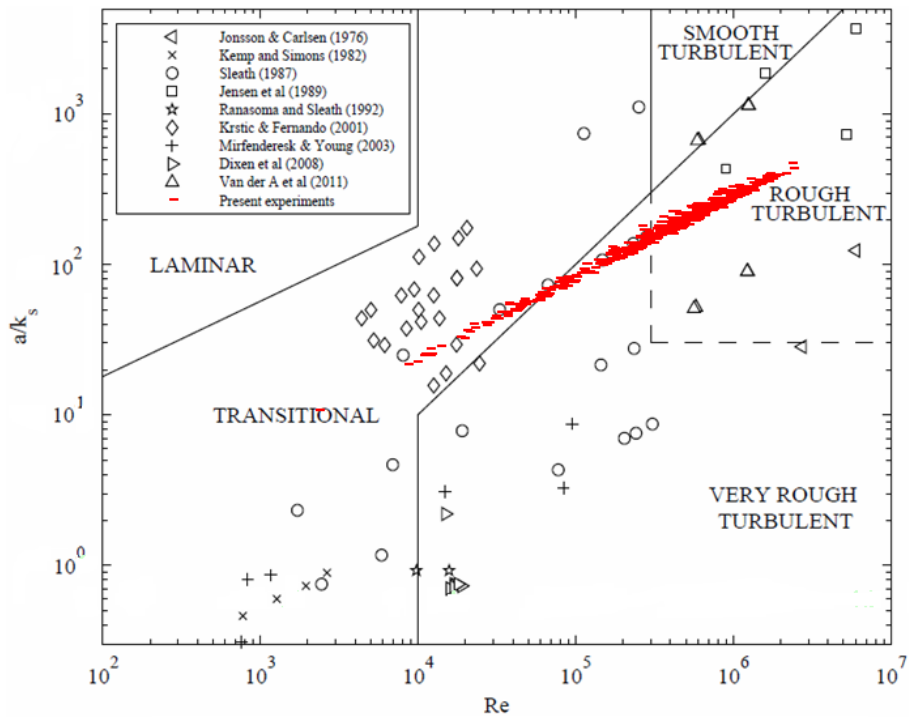
With $\kappa = 0.4$.

Figure V.6: Delineation of flow regimes showing the present experiments amongst previous fixed bed studies (adapted from **(author?)** [13], references listed therein)
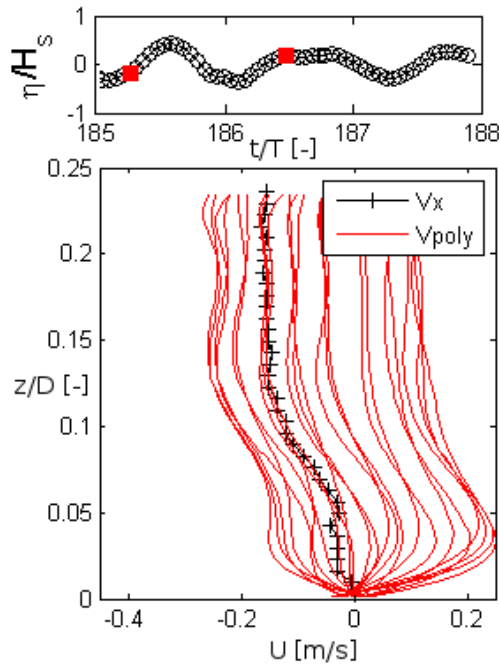

Figure V.7: Veliccity profiles at $\frac{x}{D} = 0.1$ varying with time

V.3.2.3   Flow structures along the pile

Vertical planes of velocities highlighted also the presence of alternative structures along the axis of the cylinder at the lee side. Figure V.8 shows the velocity gradient for one vertical plane. Such features have already been observed for very low values of KC ($KC = 4.5$: **(author?)** [14]; $1 < KC < 3$: **(author?)** [6]). Plotting the evolution with time of the vertical shear stress very next to the pile (at x/D=0.02) is a convenient way to detect those kind of structures (Figure V.9). The occurence conditions of those kind of structures are to be deeply examined. The first step consists in defining the KC values of the synchronized undisturbed flow. Indeed such structures are known to appear at $KC = 1$.
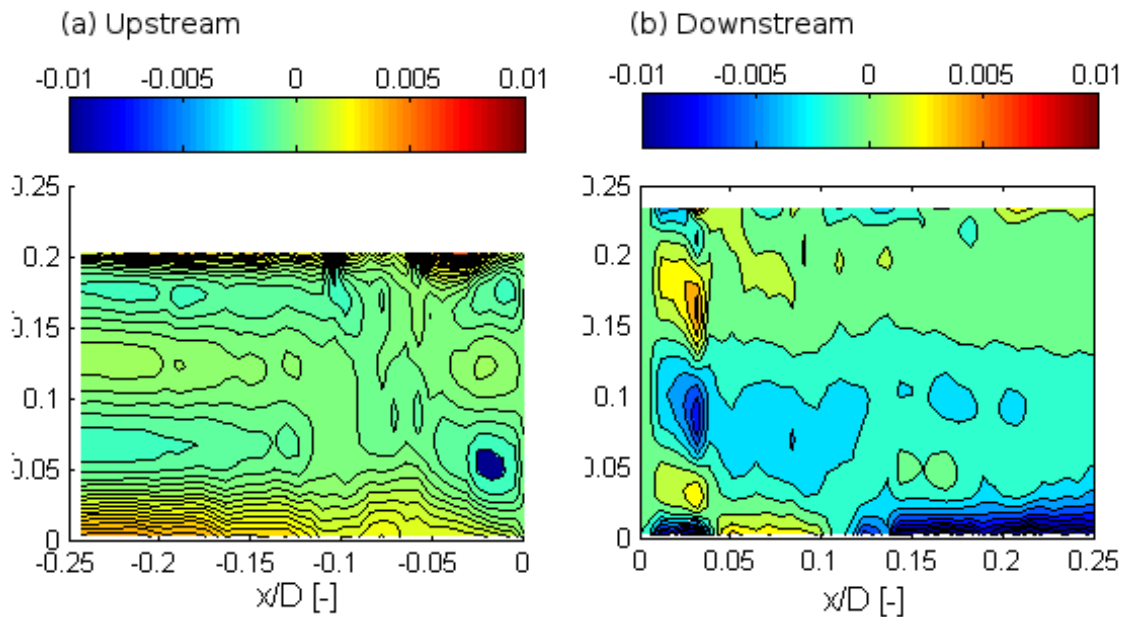

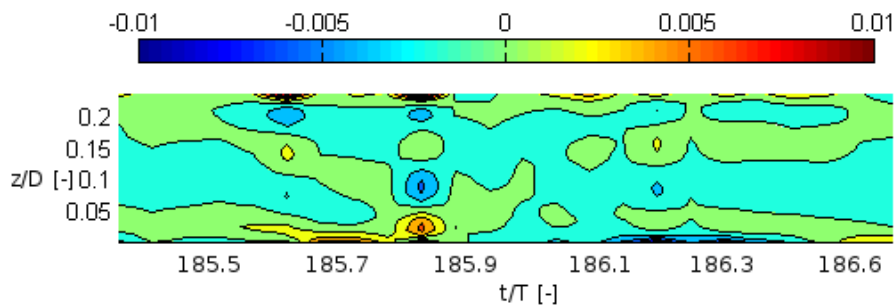Figure V.8: Flow structures along the pile - H_s=5m ; T_p=8s

Figure V.9: Shear stress along the pile at $x/D = 0.02$ and for $t/T = [185.3; 186.5]$

V.3.2.4   Upstream jets

Next to the bottom, jets were generated upstream the pile (Figures V.10 - a, V.11 - a). These are strong velocities regions that impacts the bottom until $D/4$. The jets generate a kind of drag effect that clearly appears on shear stress fields (Figures V.10 - b, V.11 - b). The dimensions and appeerence conditions have to be quantified and might be associated to scour houle dimensions.

V.3.2.5   Vortex at the lee side of the pile

Horseshoe vortex and lee-wake vortices are supposed to occur around a pile for values of $KC > 6$ [11]. Considering lower values of KC, no flow separation might happen (Figure V.12). However, the present
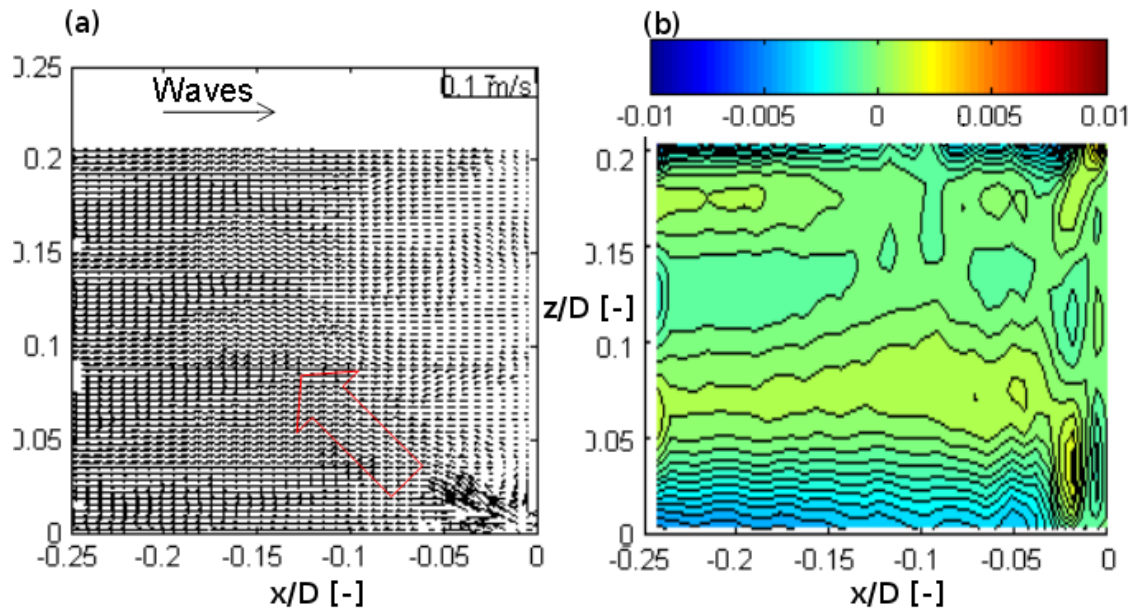
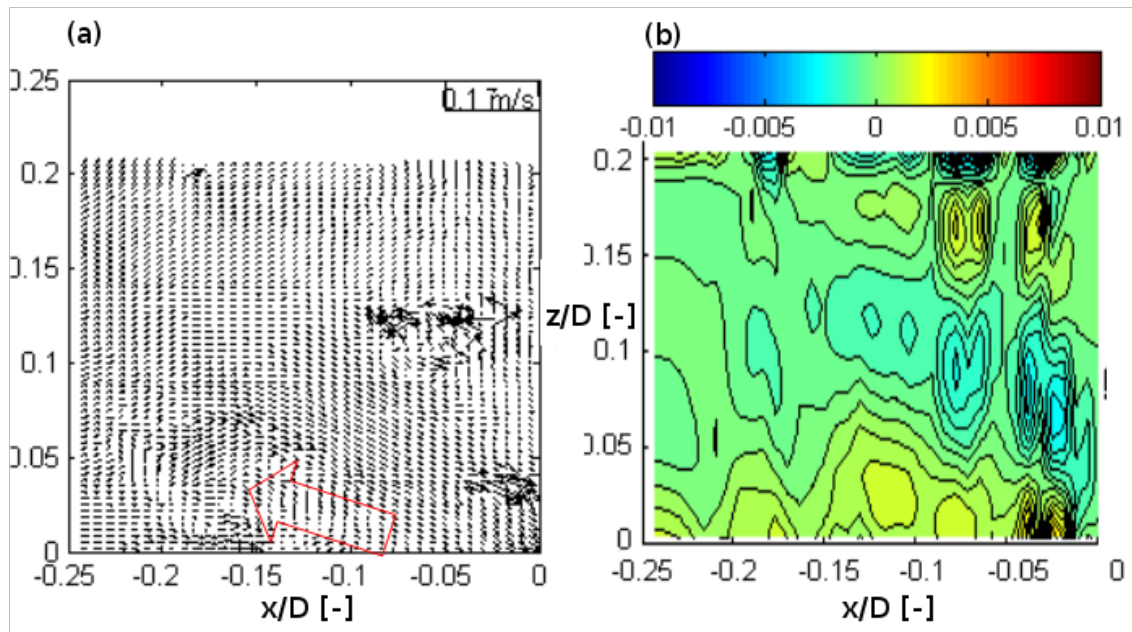Figure V.10: Velocity jets upstream the pile at $t/T =$ (a) velocity field ; (b) shear stress field

Figure V.11: Velocity jets upstream the pile at $t/T =$ (a) velocity field ; (b) shear stress field

tests reveal that eddies were generated downstream. Those vortices were clearly seen on the vertical sheet measurements of PIV. They also briefly appear on horizontal planes (especially at $z/D=0.05$), as a signature of strong velocities next to the pile.
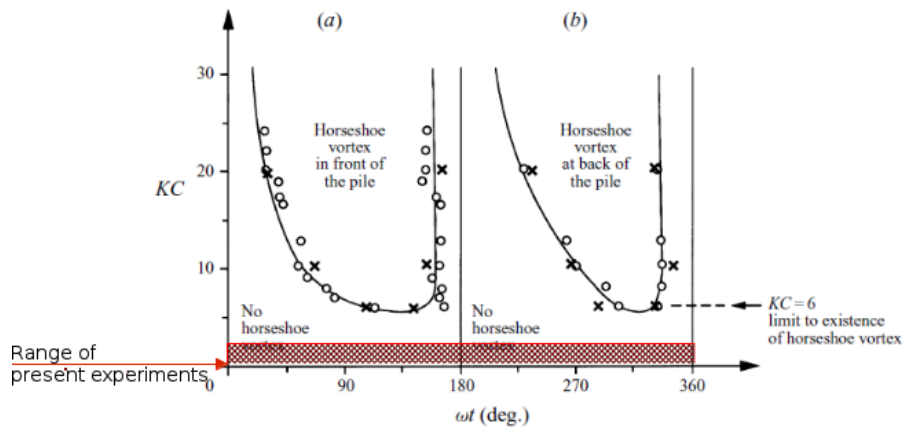

Figure V.12: Existing references for horeshoe vortex appearance

The generation of those eddies is quite surprising because $KC < 2$. The presence of vortex has been reported (Figure V.13). Statistics of the associated local flow characteristics were performed. No dependence were found between vortex generation and the local flow (Figure V.14). But it appears that the apparition of the vortex depends on the historic of the flow. When considering the 3 previous waves, vortex generation is related to the strongest waves of the sample. We can suppose that the generation of the vortex is related to a sequence of waves including strong conditions. This is an important result because severe wave conditions might induce sediment motion and the presence afterwards of a vortex, locally increasing bottom shear stress, might generate scour. The occurence of a vortex can be detected with shear stress calculation (Figure V.15). And the impact of those vortex on the bottom is to be evaluated. Comparison between shear stress induced by the vorticies and shear stress obtained for the undisturbed flow (without any pile) have to be performed. Complementary tests are in progress to finalize this deep analyse of the impact of the pile on the flow next to the bottom.
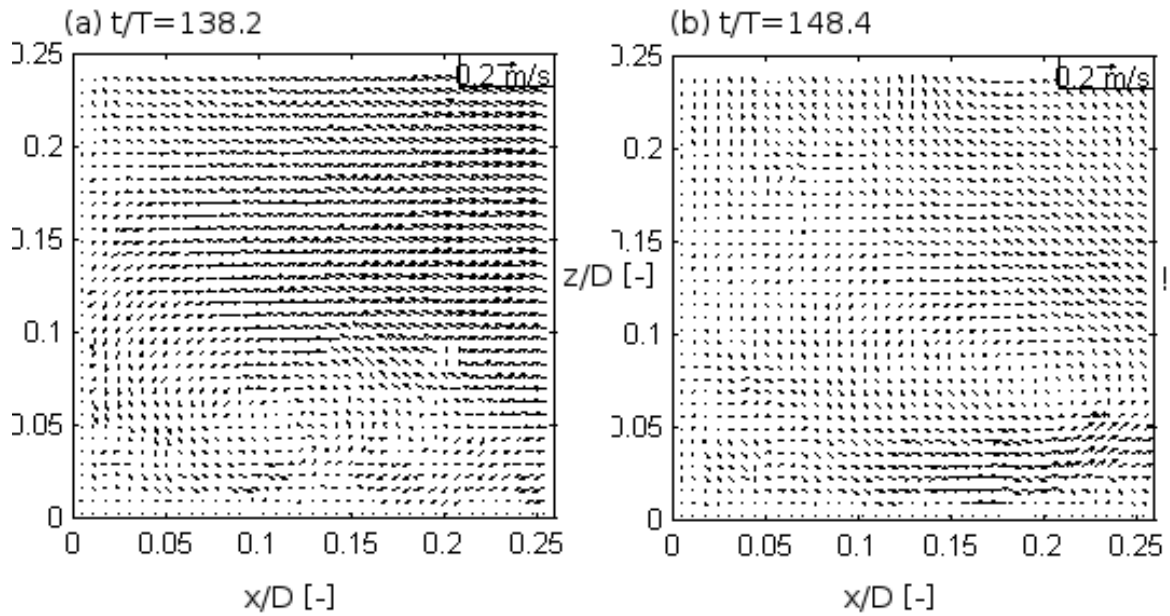
Figure V.13: Vortex visualisation downstream the monopile at low KC values (a)$t/T = 138.2$;(b)$t/T = 148.4$

Figure V.14: Steepness distributions for waves considering : the entire test (blue), the waves where vortex appear (purple), the two waves before the wortex appear (yellow)
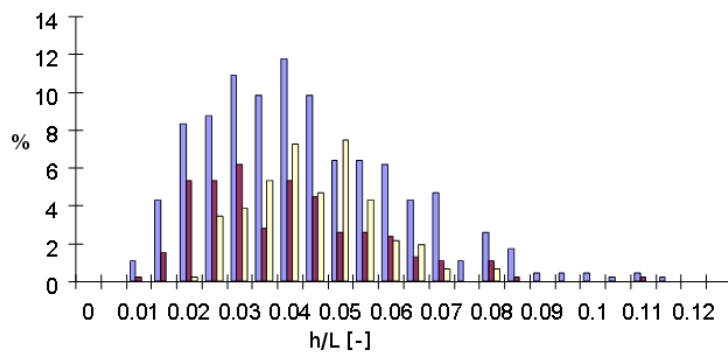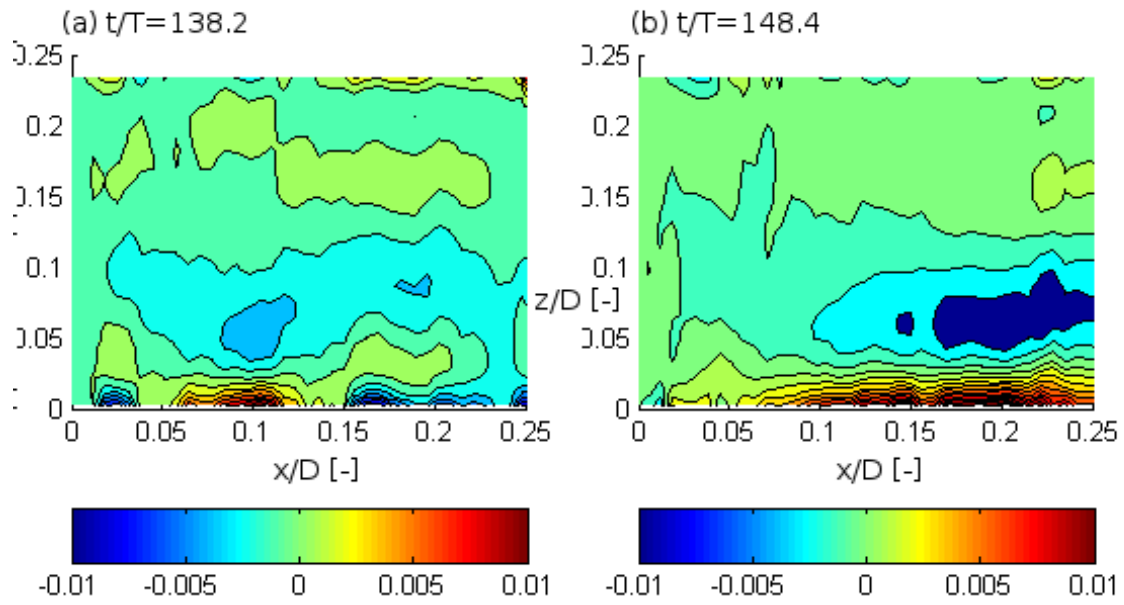
Figure V.15: Shear stress with vortex visualisation downstream the monopile at low KC values (a)$t/T = 138.2$;(b)$t/T = 148.4$
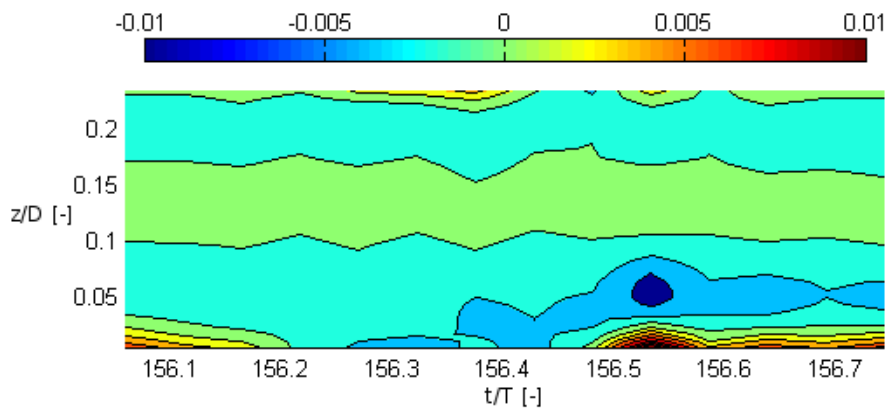

Figure V.16: Signature on shear stress of a vortex going through the vertical profile at $x/D = 0.1$ and for $t/T = [156.1; 156.8]$

V.4 Conclusions

The present results are preliminary findings and further post-processing and quantitative analysis will provide a deeper insight into the flow velocity increase in the vicinity of the cylinder and near the bed. This in turn will provide estimates of increase in bed shear stresses due to waves only. Flow structures such as vortices and other recirculation patterns near bed were observed upstream as the wave propagates around the cylinder. Observed flow recirculation patterns up- and downstream of the cylinder may increase the stirring effect of the waves on the bed and have an influence on the sediment erosion and deposition patterns in the area, in the short and long term. The analysis of flow vector fields under irregular waves highlighted that the flow patterns are characteristics to the particular passing wave but is also highly dependent on the wave-history i.e. on the characteristics of the previous waves. Whereas in the regular wave case, flow patterns are repeated with each wave. The experiments and results presented in this paper are due only to wave forcing. The present study is embedded into OFELIA which has a wider scope to include experiments comprising currents and sediment transport. It is the aim of the project to put together the findings from parallel experimentation and numerical modeling to improve understanding of the hydrodynamic and sedimentary processes around a cylinder.

V.5 Acknowledgments

References

[1] Energies marines: quelles perspectives de cration de valeur en france? Technical report, Syndicat Syndicat des Energies Renouvelables, April 2014.

[2] B Dargahi. The turbulent flow field around a circular cylinder. *Experiments in Fluids*, 12:1–12, 1989.

[3] Department of Energy and Climate Change. Annual tables: digest of uk energy statistics (dukes), ch6: Renewable sources of energy, 2013.

[4] Y. Goda and Y. Suzuki. Estimation of incident and reflected waves in random wave experiments. In *Proceedings of the 15th International Conference. Coast Eng, (ICCE'76), ASCE*, pages 828–845, 828-845, 1976.

[5] Derek G Goring and Vladimir I Nikora. Despiking acoustic doppler velocimeter data. *Journal of Hydraulic Engineering*, 128(1):117–126, 2002.

[6] H. Honji. Streaked flow around an oscillating circular cylinder. *J. Fluid Mech.*, 107:509–520, 1981.

[7] K. M. Lam, J. C. Hu, and P. Liu. Vortex formation processes from an oscillating circular cylinder at high keulegan-carpenter numbers. *Phys. Fluids.*, 22:015105, 2010.

[8] Nobuhito Mori, Takuma Suzuki, and Shohachi Kakuno. Noise of acoustic doppler velocimeter data in bubbly flows. *Journal of engineering mechanics*, 133(1):122–125, 2007.

[9] D. Myraugh. A rational approach to wave friction coefficients for rough, smooth and transitional turbulent flow. *Coastal Eng.*, 13:11–21, 1989.

[10] M. Ozgoren and D. Rockwell. Interaction of a deepwater wave with a vertical cylinder: effect of self-excited vibrations on quantitative flow patterns. *J. Fluid Mech.*, 572:189–217, 2007.

[11] BM Sumer, N Christiansen, and J Fredsøe. The horseshoe vortex and vortex shedding around a vertical wall-mounted cylinder exposed to waves. *Journal of Fluid Mechanics*, 332:41–70, 1997.

[12] B.Mutlu Sumer, Richard J.S Whitehouse, and Alf Tørum. Scour around coastal structures: a summary of recent research. *Coastal Engineering*, 44(2):153–190, December 2001.

[13] D.A. Van der A, A.G. ODonoghue, T.and Davies, and J.S. Ribberink. Experimental study of the turbulent boundary layer in acceleration-skewed oscillatory flow. *Journal of Fluid Mechanics*, 684:251–283, 2011.

[14] Y. Yang and D. Rockwell. Wave interaction with a vertical cylinder: spanwise flow patterns and loading. *J. Fluid Mech.*, 460:93129, 2002.

[15] U.C.E. Zanke, T.W. Hsu, A. Roland, L. Oscar, and D. Reda. Equilibrium scour depths around piles in noncohesive sediments under currents and waves. *Coast. Eng.*, 58:986991, 2011.

VI

Regional numerical modelling of offshore monopile wind turbine impacts on hydrodynamics and sediment transport

A. Rivier, A.C. Bennis, G. Pinon, V. Magar, M. Gross

VI.1   Introduction

Offshore wind farms are planned to be built in the English Channel along both French and English coasts in the coming years. Offshore monopile foundation modifies hydrodynamics and sediment transport at local scale and also at regional scale. Their impacts on sediment transport have been for instance observed in North Sea by CEFAS [7], Department of Energy and Climate Change [10] and Vanhellemont and Ruddick [28]. Computational fluid dynamics models (CFD) are able to represent complex fluid structure around a monopile [e.g. 26, 23, 14]. However the computational time of this technique doesn't allow studies at a regional scale. Analytical expressions of drag [e.g. 11] or with finite element models in two dimensions [e.g. 2] could be used in impact assessement studies to evaluate the monopile effects on hydrodynamics. The first method is simplistic and a three-dimensional analysis is needed to known the vertical structure of velocity and in particular the near-bed velocity which is essential to assess the sediment transport. Christie et al. [8] show for instance the differences of velocity fields and bed evolution around a monopile foundation between a two-dimensional and a three-dimensional model. The foundation could also be represented by increasing the apparent roughness at pile location [15], or by adding a drag source term in the momentum equations [19]. The impact of offshore wind farm on sediment transport is often assessed using directly outputs from hydrodynamical model to estimate the shear stress exceedance, with empirical equation describing mobility of sediment [15, 19]. However this method is not able to capture the process of advection of the resuspended sediment, nor its deposition downstream of the monopile.

The aim of this study is to estimate the impact of the monopile on the hydrodynamics and sediment transport using a three-dimensional regional model like MARS, which solves circulation [16] and sediment transport [17] equations and allows reasonable calculation time at a regional scale, and to find a parametrization which is able to reproduce properly the modifications of hydrodynamics and sediment dynamics due to monopiles. The study focuses on the area of the future wind farm of Courseulles-sur-Mer (Calvados, France), where the bed is composed of sand and gravels and the water depth is between 20 and 30 meters (m). Currents induced by tide are strong, reaching speeds of 1 meter per second (m/s) during medium spring tides and 1.3 m/s during highest spring tides. The influence of waves is weaker in the wind farm site, because the area is protected against waves from the Atlantic Ocean by the Cotentin Peninsula.

In this work, monopiles are modelled using two approaches in this work. In the first one, monopiles are explicitly solved in the the mesh and are represented as dry points. In the second one, a subgrid parametrization is used by adding source terms in the momentum and turbulence equations. These methods are first tested on test-cases having characteristics close to the Courseulles-sur-Mer site. Then

they are applied in the real case using nested domains.

VI.2 Model description

The regional hydrodynamical model MARS3D [16], which solves the momentum equations under the Boussinesq and the hydrostatic approximation, is applied in this study. Vertical mixing is solved using the generic length scale formulation [27]. A sediment transport module solving the equation of advection-diffusion in the water column is included in MARS3D [17].

As explained above, the influence of the monopile is taken into account using two methods. In the first one, the monopiles are solved explicitly. They are incorporated in the mesh and are treated as dry cells in the model. In the second one, the impact of the foundations on the environment is parameterized. The drag force exerted on the flow by the monopile is incorporated in the model by adding an extra source term in the momentum and turbulence equations. For instance, source terms are added in the momentum and also in turbulence equations to model the impact of vegetation on air-flow [18, 24] and on water-flow [25, 6, 4, 20], and to model the impact of tidal turbines on hydrodynamics [22].

The drag force per unit area, $\mathbf{F_d}(Fu_d, Fv_d)$, induced by the monopile can be expressed in the x and y directions as:

$$Fu_d(z) = -\frac{1}{2}\frac{\rho_0 C_d(z)D}{\Delta x \Delta y}\|\mathbf{u}_\infty(\mathbf{z})\|u_\infty(z) \tag{VI.1}$$

$$Fv_d(z) = -\frac{1}{2}\frac{\rho_0 C_d(z)D}{\Delta x \Delta y}\|\mathbf{u}_\infty(\mathbf{z})\|v_\infty(z) \tag{VI.2}$$

where $C_d(z)$ is the drag coefficient, D is the diameter of the pile, $\mathbf{u}_\infty(u_\infty, v_\infty)$ is the undisturbed current velocity upstream of the pile, Δx and Δy are the horizontal grid sizes and $\|.\|$ is the l^2 norm. These terms, divided by the density ρ_0, are added to the right hand side of momentum equations expressed in a Cartesian coordinates system. The drag coefficient $C_d(z)$ could vary depending of the vertical position. In this study C_d is five time higher in the cell closest to the bottom to take into account the higher drag induced nearbed by the the junction of the bed and the cylinder.

The turbulence equations become:

$$\frac{\partial k}{\partial t} + u\frac{\partial k}{\partial x} + v\frac{\partial k}{\partial y} = \frac{\partial}{\partial z}\left(\frac{\nu_V}{s_k}\frac{\partial k}{\partial z}\right) + P - \epsilon + \frac{\|\mathbf{u}_{\infty(\mathbf{z})}\|\|\mathbf{F_d}(\mathbf{z})\|}{\rho_0} \tag{VI.3}$$

$$\frac{\partial \psi}{\partial t} + u\frac{\partial \psi}{\partial x} + v\frac{\partial \psi}{\partial y} = \frac{\partial}{\partial z}\left(\frac{\nu_V}{s_\psi}\frac{\partial \psi}{\partial z}\right) + \frac{\psi}{k}\left(C_1 P - C_2\epsilon F_{wall} + C_2\frac{\|\mathbf{u}_{\infty(\mathbf{z})}\|\|\mathbf{F_d}(\mathbf{z})\|}{\rho_0}\right) \tag{VI.4}$$

where k is the turbulent kinetic energy, ψ is a generic length scale, P and B represent the effects of shear and buoyant production, C_1, C_2, C_3, s_k, s_ψ are empirical constants. Buoyancy is neglected in this study ($B = 0$). For a $k - \epsilon$ turbulence model, they are adopted as follows $C_1 = 1.44$, $C_2 = 1.92$, $s_k = 1$, $s_\psi = 1.3$ and F_{wall} is equal to 1 [27].

Horizontal viscosity depends on the size of the mesh and it is expressed as:

$$\nu_H = f_{visc} \cdot 0.01 \cdot \Delta y^{1.15} \tag{VI.5}$$

with f_{visc} a coefficient ranging between 1 and 17 and Δy being the size of the cell in y-direction.

The distance between the pile and the location (i_∞, j_∞) where the velocity is considered undisturbed $(\mathbf{u}_\infty)$ was determined using the dry points approach for a pile with a diameter of 6 m and input velocities ranging between 0.3 and 1.2 m/s. Velocities were considered undisturbed when they are superior or equal to 99 % of the input velocity. Being based of these tests, the velocity is taken 90 m upstream the pile to estimate $\mathbf{u}_\infty$. In this study only transport of sediments by suspension are considered. The thickness of the bed could change during the simulation but the bathymetry couldn't change.

Modifications of the hydrodynamics and sediment dynamics induced by monopile foundations will be presented using the relative difference which is expressed for the variable V as :

$$\Delta V^{rel} = \frac{V_{monopile} - V_{ref}}{V_{ref}} \tag{VI.6}$$

where $V_{monopile}$ and V_{ref} are respectively the values of the variable simulated with monopiles (using dry points or parametrization methods) and without monopile.

VI.3 Applications

VI.3.1 Test-cases

VI.3.1.1 Configurations

Several test-cases were studied to evaluate the capacity of the hydro-sedimentary model to represent the monopile behaviour using both approaches. The test-cases allowed for variations in the velocity directions and speed, the diameter of the monopile, the grain size diameter and the origin of sediment (bed or input from boundaries). The hydrodynamical conditions used are chosen to be close to Courseulles-sur-Mer (Calvados) area where a wind farm are planned to be built in 2018.

Three test-cases are presented here. In the first and the second test-cases, the horizontal resolution is 3 m, the time step is 0.5 s, the water depth is 30 m, a constant eastward current is applied at the boundaries and the bed, with an initial thickness of 1 m, is composed of homogeneous sand with a diameter equal to 250 μm. In the first test-case, the input velocity is 0.6 m/s, the diameter of the monopile is 6 m and the water column is divided into 15 uniform layers. In the second test-case, the input velocity is 0.5 m/s, the diameter of the monopile is 15 m and the water column is divided into 25 uniform layers. The third test case is similar to the second test case, excepted that sediment is very fine sand (diameter of 65 μm instead of 250 μm), presents initially only in the water column (instead in the bed) and is applied at the boundaries with a concentration of 5 mg/l.

The order of magnitude of Reynolds number is 10^6. In agreement with measurements made by Achenbach [1] for this range of Reynolds numbers and with the value taken by Rennau et al. [21] in the Baltic Sea, $C_d(z)$ is chosen equal to 0.65 in the water column, except for the cell closest to the bottom where it is five time higher. The horizontal viscosity is uniform and equal to 5.3 $10^{-2} \mathrm{m}^2.\mathrm{s}^{-2}$. The roughness length z_0 is taken equal to 3.5 10^{-4} m as suggested by Soulsby(1997) for sand and gravel.

VI.3.1.2 Results

Figure VI.1 shows various variables which characterise the hydrodynamics and the sediment dynamics. The parametrization method (right) reproduces well the patterns of these variables obtained with the explicit method (left). With both approaches, the current speed decreases in front of the monopile and increases at the side edge as expected. A wake is formed downstream of the monopile. The pattern and the intensity of the relative difference of velocity induced by the monopile is not the same close to the bed and at the surface, showing the importance to use a model in three dimensions. Barotropic vorticity shows the vortices which are created behind the monopile. The presence of the monopile increases the bed shear stress at the side edge and decreases it in front of, and downstream of the cylinder, in agreement with the fields of near-bed current velocity. This spatial distribution is in agreement with Dargahi [9], Roulund et al. [23] and Dixen et al. [12]. The increase of the bed shear stress leads to the erosion of the bed with an increase of the suspended sediment concentration and a decrease of the bed thickness at the side edge. The bed shear stress in the presence of the monopile is not high enough downstream of the monopile to erode the bed at this location. Sediments eroded close to the monopile deposit upstream and downstream, especially at the side edge of the wake. This pattern is representative of the bed thickness at the first steps of erosion. The use of a morphodynamical module is needed to include changes of bathymetry and calculate the new bed shear stress which varies when the bed starts to be eroded [e.g. 12]. It is noticed that the patterns of the relative difference of these variables are more symmetric with the parametrization than with the explicit method. This is because the dry points approach introduces instabilities in the model.

In the second test case (Fig. VI.2), simulations are run with a higher Reynolds number ($Re = 7.5 \times 10^6$) and a larger monopile ($D = 15$ m) which is included in 21 cells instead of 4 for the first test case. Vortices appear downstream of the monopile, leading to a periodical increase of the bed shear stress in the wake of the monopile (Fig. VI.2, top). The bed is eroded with ripples because of these oscillations (Fig. VI.2, bottom). This pattern of deposition downstream of the monopile with ripples is in agreement for instance with measurement shown in [13].

In the third test-case, very fine sand is introduced in all the water column and at the boundaries. These very fine sediments are still in suspension at the surface downstream of the monopile : a turbid wake appears 5 (Fig. VI.3). This result is in agreement with satellite observations by remote sensing in London array [28].

The dry points strategy is considered here as the reference method. However, velocities obtained with this method still have to be validated. The width of the wake predicted with this method is compared
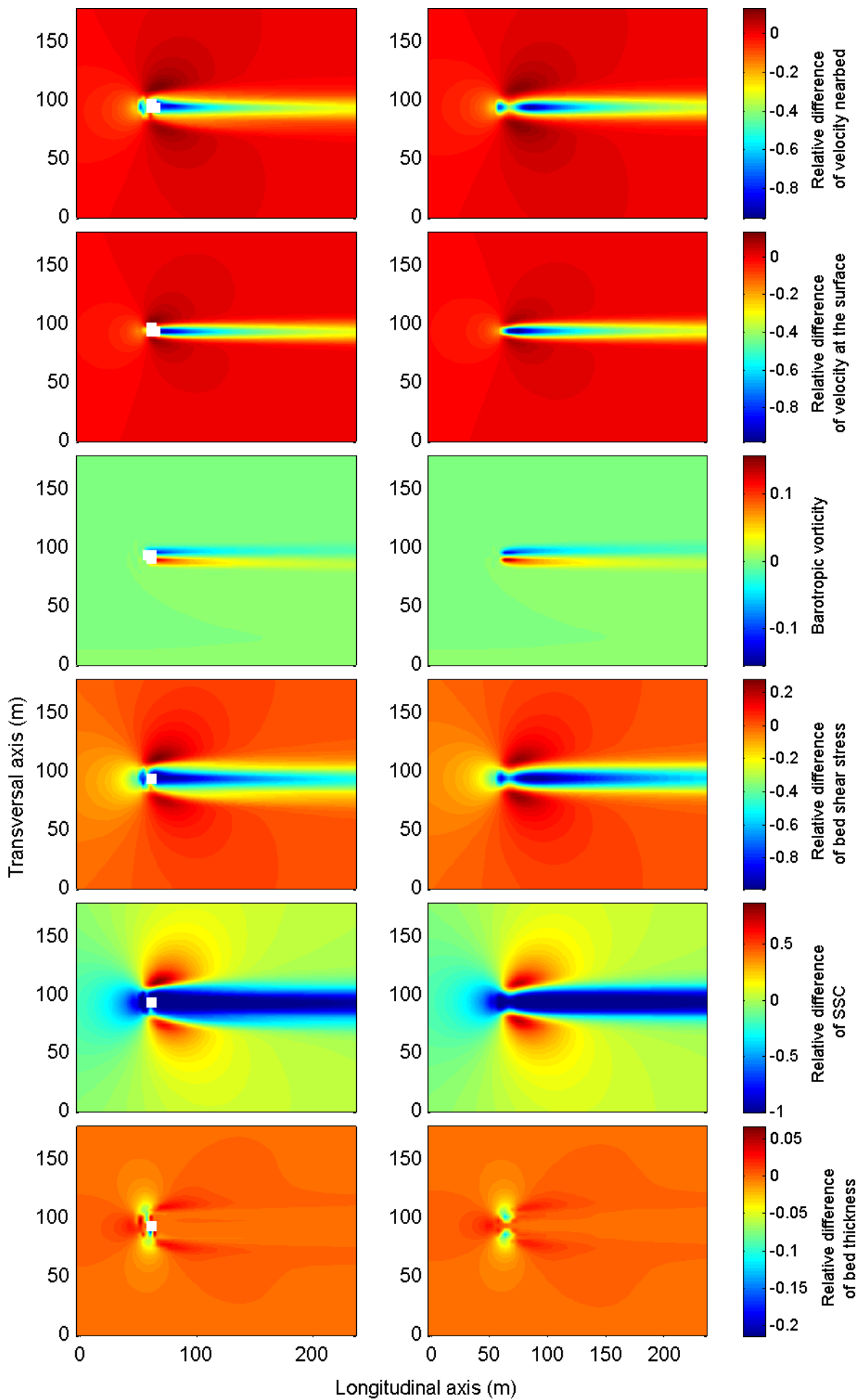
Figure VI.1: Relative difference of magnitude of velocity near-bed and at the surface, barotropic vorticity, relative difference of bed shear stress, suspended sediment concentration near-bed and bed thickness after 12h of simulation using explicit resolution (left, dry cells are in gray) and parametrization method (right).
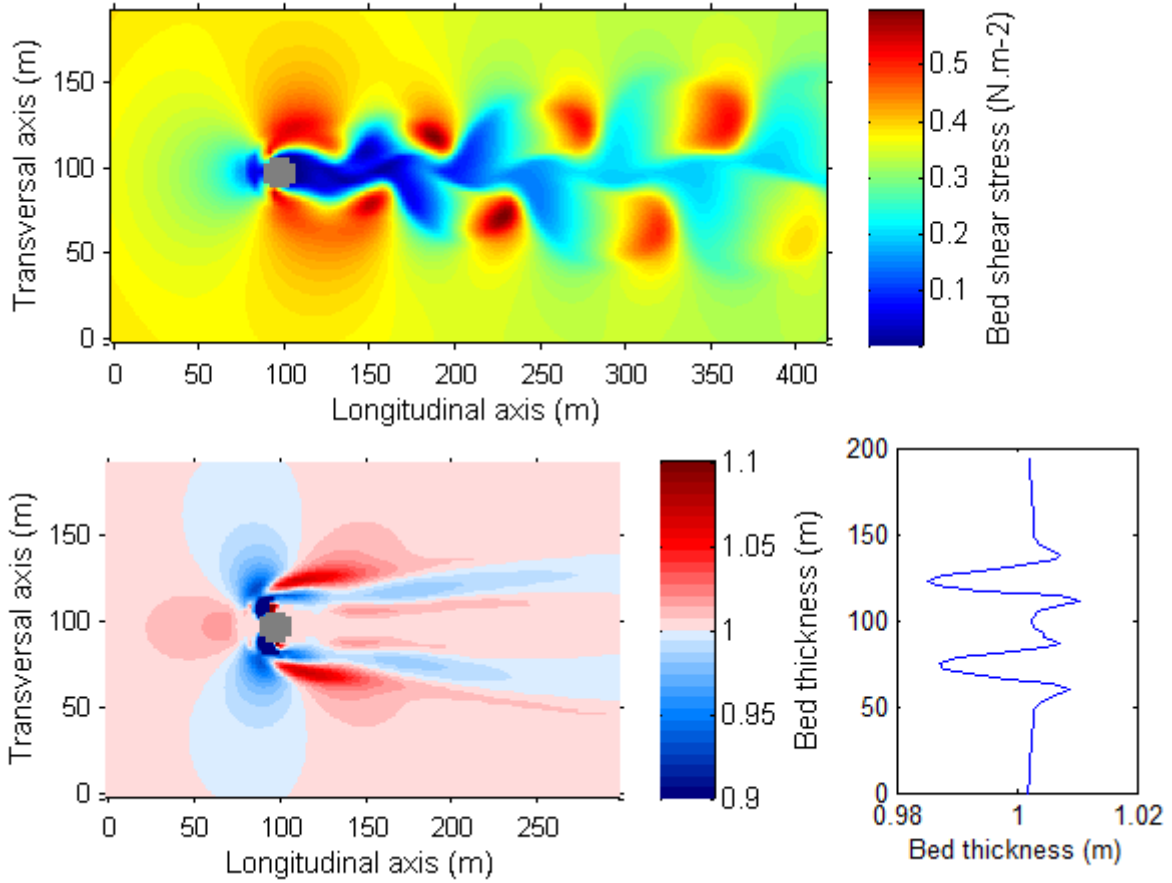
Figure VI.2: Bed shear stress (top, N.m^{-2}) and bed thickness (bottom, m, horizontal field at the left and transversal profil 100 m behind the monopile) using a monopile with a diameter of 15 m, an input velocity of 0.5 m.s^{-1} and a sand diameter of 250 μm after 12 hours of simulation using explicit resolution (dry cells are in gray).

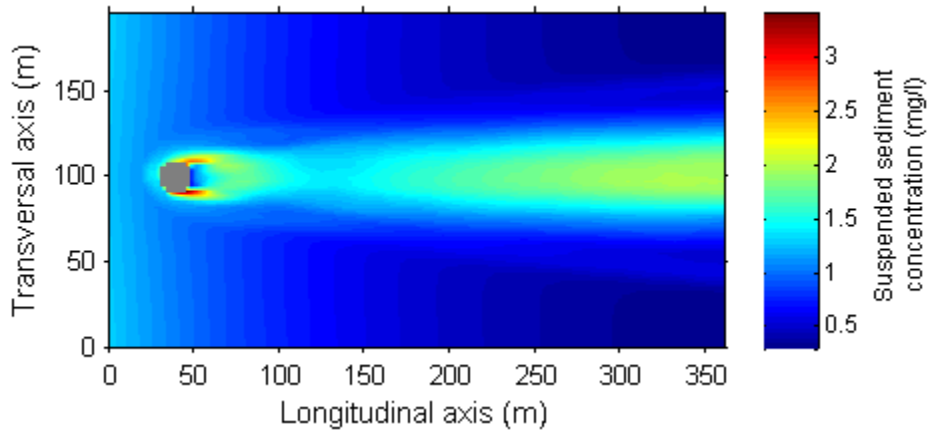
Figure VI.3: Suspended sediment concentration (mg/l) at the surface using a monopile with a diameter of 15 m, an input velocity of 0.5 m.s^{-1} and a sand diameter of 65 μm using explicit resolution (dry cells are in gray).

with experimental measurements described in Baelhaq [3], following a Froude similarity criterion. The intensity of the streamwise component of velocity across the flume near the surface is correctly reproduced. The length of the wake numerically modelled is also compared to the experimental data obtained in the wave and current flume at Plymouth University during this OFELIA Project using Froude similarity.

Froude similarity doesn't allow Reynolds similarity and horizontal viscosity is artificially increased in the model ($\nu = 3.5 \times 10^{-6} \text{m}^2.\text{s}^{-2}$) to soften turbulence created because of a higher Reynolds number in numerical modelling than in experiments. The evolution of the streamwise component of velocity downstream of the monopile is similar between measurements obtained in current-only experiments and modelling when using this horizontal viscosity coefficient .

VI.3.2 Courseulles-sur-Mer

VI.3.2.1 Configurations

The regional model MARS is applied in three dimensions in a domain including the future offshore wind farm of Courseulles-sur-Mer (Fig. VI.4) during a medium tide on the 11th of November 2011. Five nested domains are used to allow a high resolution and take into account explicitly the monopile in the mesh. The horizontal resolutions are around 243 m for domain 0 (red grid), 81 m for domain 1 (green grid), 27 m for domain 2 (pink grid), 9 m for domain 3 (blue grid) and 3 m for domain 4 (brown grid). Time steps are 20 s for domain 0, 10 s domain 1, 5 s for domain 2, 1 s for domain 3 and 0.5 s for domain 4. Data from SHOM (French Navy) force the sea surface height for domain 0 and data from the previous domain are used for the other domains Zero velocity gradients are imposed along open boundaries for domain 0 and Dirichlet conditions are used for velocities for the other domains. Only the domain 4 is solved in three-dimensions with 15 levels in the water column and with sediment transport module. Four monopiles are placed in this last domain with a positioning similar to the configuration of Courseulles-sur-Mer wind farm using both approaches. Waves are neglected in this study because the action of current is globally stronger at this location.

In the regional simulation case, the horizontal viscosity had to be increased to avoid numerical instabilities. The coefficient f_{visc} is taken equal to 10 which leads to a horizontal viscosity of 0.37 $\text{m}^2.\text{s}^{-2}$ for the last domain of this configuration. $C_d(z)$ has to be increased to 1 to reach the same order of magnitude for the velocity in dry points method and parametrization method while keeping the same pattern. This is due to the increase of the horizontal viscosity which reduces and softens the effect of drag force on the flow and the drag coefficient. $C_d(z)$ is still five time higher in the cell closest to the bottom.

VI.3.2.2 Results

The bottom of figure VI.4 shows the relative difference of the depth-averaged velocity due to four monopiles located in the future wind farm located off Calvados during the flow when the magnitude of velocity is maximum. The modification of the current velocity close to the monopile are similar to those obtained in the test-cases. The deficit of velocity due to the monopile reaches the following monopile which is located 950 m dowtream. This length of wake is in agreement with the length of turbid wake observed in London array by remote-sensing [28]. The decrease of velocity is above 10 % up to around 600 m downstream. The parametrization and the explicit resolution have similar result, the relative difference with the parametrization being a little bit lower.

One hour later, the wakes and the rows of wind turbines are aligned (Fig. VI.5). Figures VI.5 and VI.6 show the near-bed velocity at this time. The patterns simulated around the first monopile (Fig. VI.6, top) are in agreement with pattern found in test-case (Fig. VI.1) with both approaches. However results differ around the monopile located downstream. The increase of velocity at the side-edge and the increase in front of the monopile are lower. These changes of velocity fields lead to the modifications of the bed shear stress, and by consequence to the quantity of sand eroded and to the concentration of suspended sediment (Fig VI.7). Modifications are stronger for the relative difference of suspended sediment concentrations in comparison to the relative difference of near-bed velocity because the erosion flux is a function of the square of the nearbed velocity. However the wake behind the monopile is still similar for both monopile. During slack waters, when the current direction change, wakes don't reach the monopile from the other rows.

Figure VI.8 shows the relative difference of bed thickness after 12 hours around a monopile located in the future wind farm (monopile located on the bottom left-hand side in Fig. VI.4). Results with both approaches are similar. The bed is eroded at the side edge of the monopile in the same manner as for test cases with a fixed current. Because of the tidal cycle, sediments deposit alternately at the left and at the right side of the monopile. The pattern of deposition is not exactly symmetric because the intensity of the flow and ebb are not the same at this location. Erosion and deposition are higher close to the monopile with the parametrization in comparison with the dry points method.
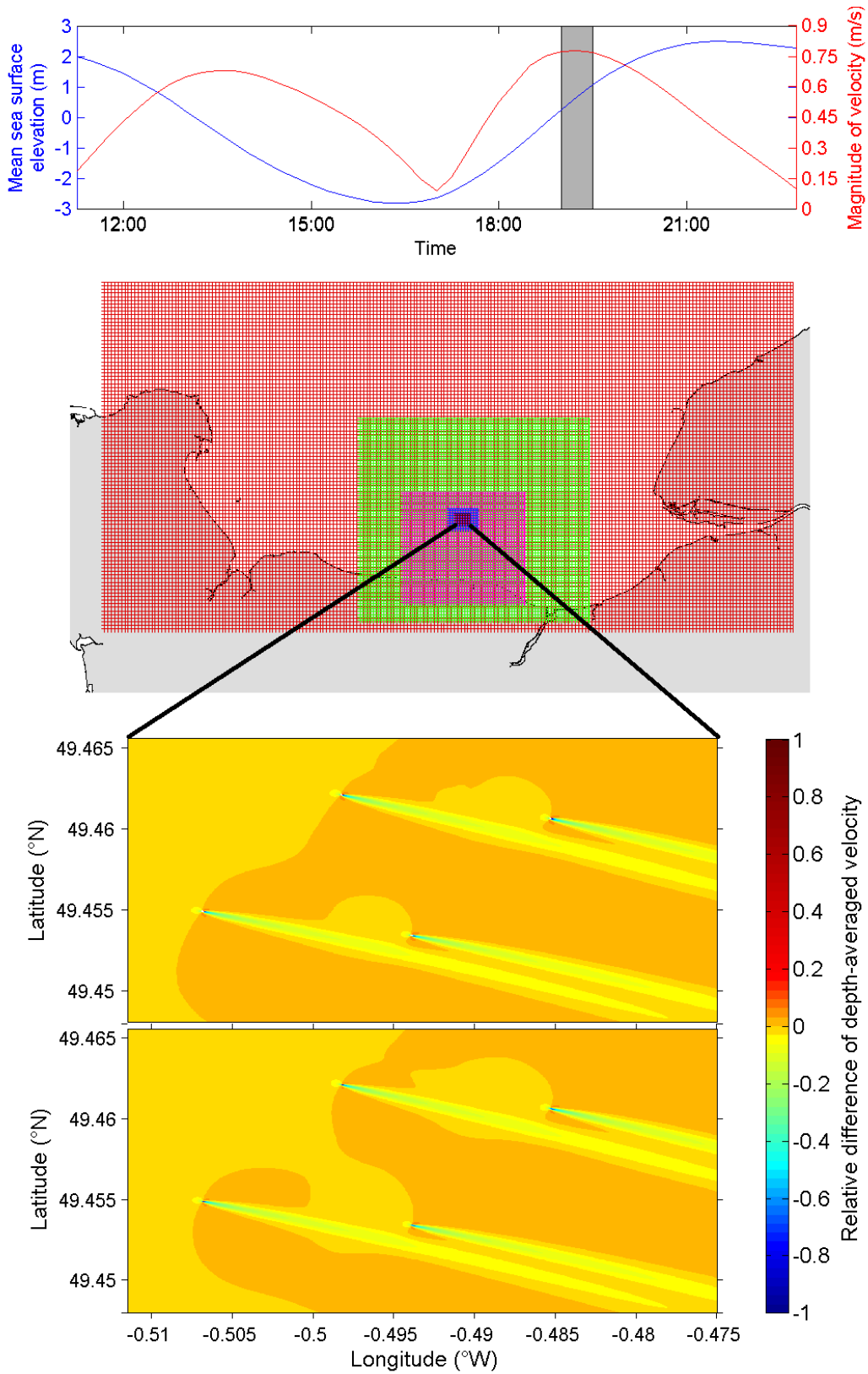
Figure VI.4: Sea surface heigh and magnitude of current the 11th of November 2011 during the simulation, calculation domains for the regional scale and relative difference of depth-averaged velocity induced by four monopiles located at Courseulles-sur-Mer (Calvados) wind farm using explicit approach and parametrization approach at 19:30 (grey rectangular on the top figure).
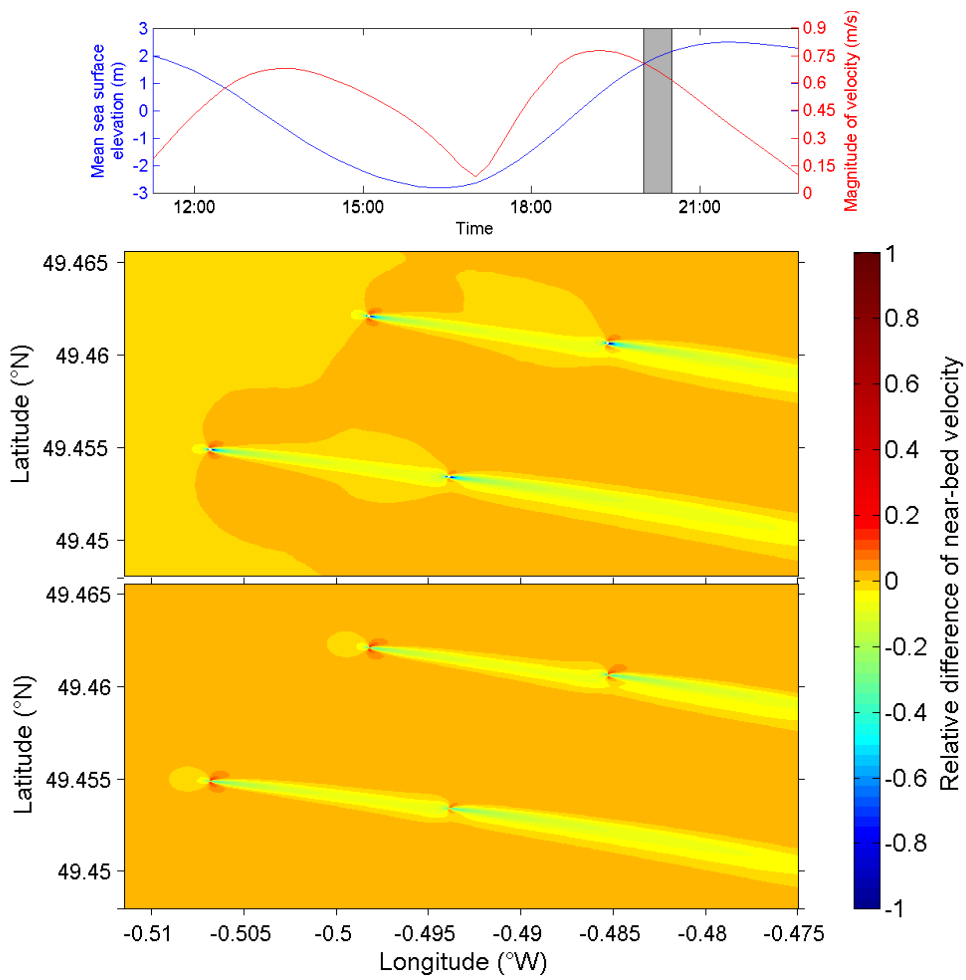
Figure VI.5: Mean sea surface elevation and magnitude of current the 11th of November 2011 during the simulation (top), and relative difference of near-bed velocity induced by four monopile located at Courseulles-sur-Mer (Calvados) wind farm using explicit approach (middle) and parametrization approach (bottom) at 20:30 (grey rectangular on the top figure).
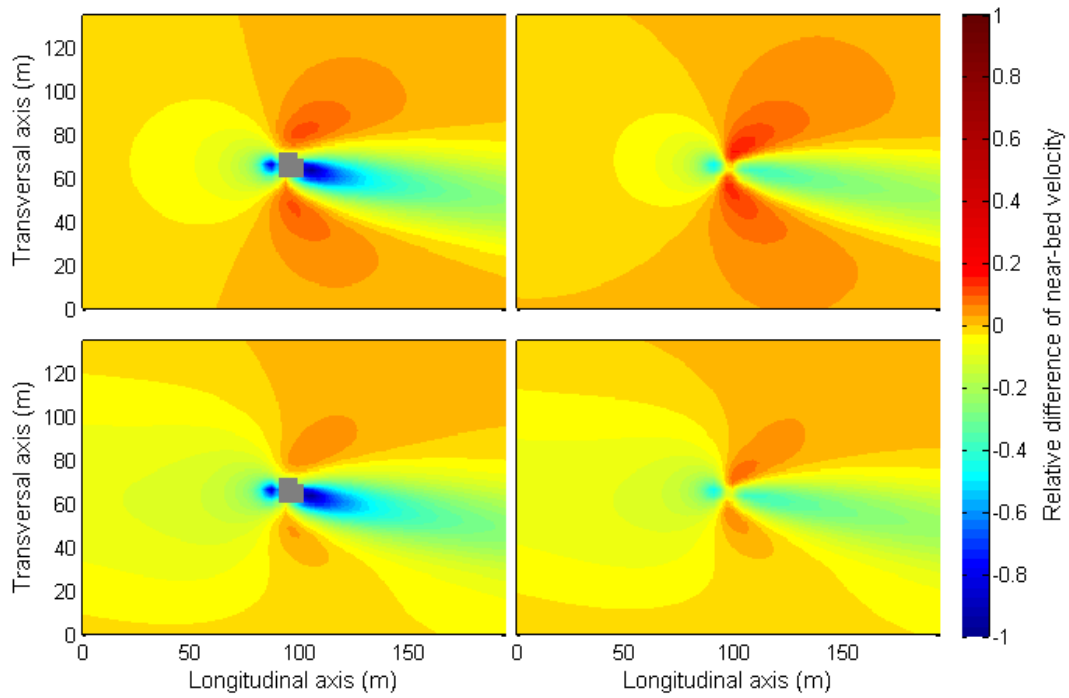
Figure VI.6: Relative difference of velocity near-bed around the monopiles located on the bottom left-hand side (top) and on the bottom right-hand side (right) in Fig. VI.5 using explicit approach (left, dry cells are in gray) and parametrization approach (right) at 20:30.
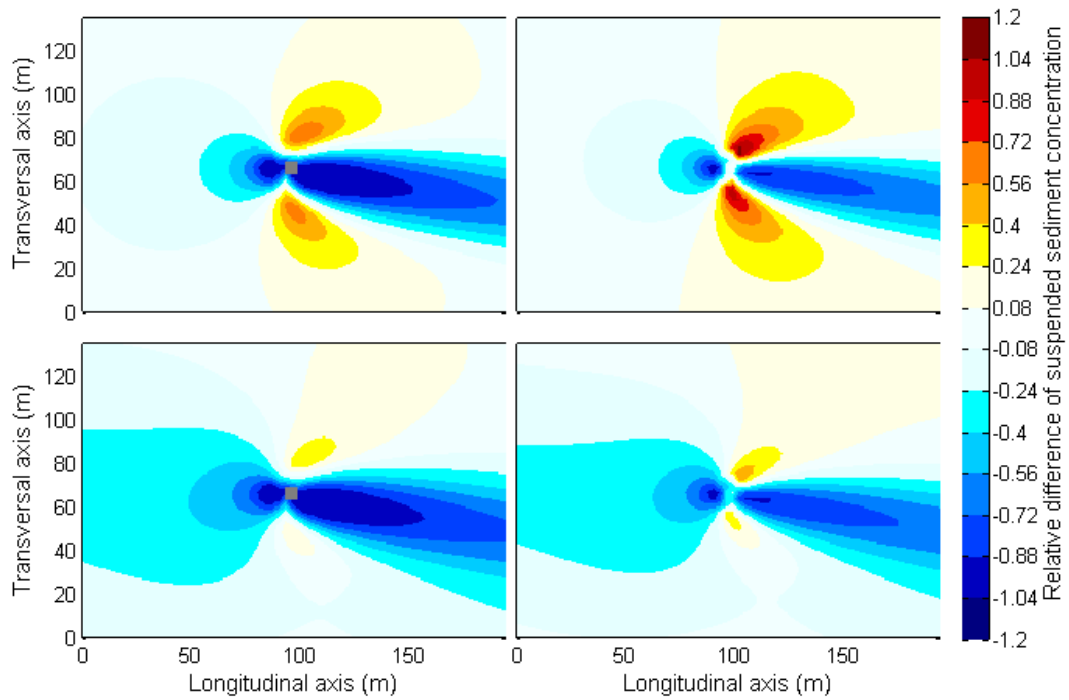

Figure VI.7: Relative difference of suspended sediment concentration near-bed around the monopiles located on the bottom left-hand side (top) and on the bottom right-hand side (right) in Fig. VI.5 using explicit approach (left, dry cells are in gray) and parametrization approach (right) at 20:30.
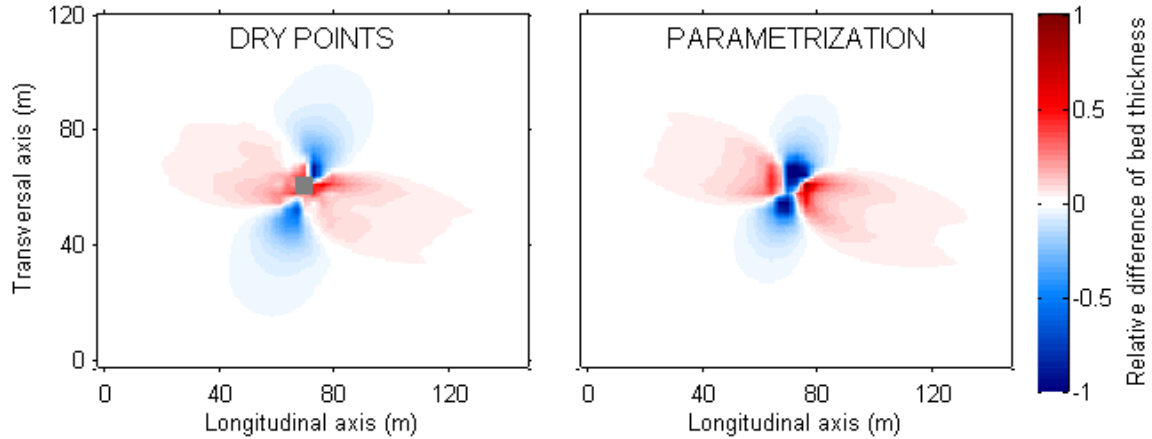
Figure VI.8: Relative difference of bed thickness induced by a monopile located in Courseulles-sur-Mer wind farm after 12 hours using explicit approach (left, dry cells are in gray) and parametrization approach (right).

VI.4   Conclusions

Two approaches to model the modifications due to monopile foundations of wind turbine on hydrodynamics and sediment transport have been tested on test-cases and in a regional configuration. The spatial distribution of velocity, and by consequence bed shear stress, simulated with the explicit resolution and the sub-grid parametrization of the monopile, are similar and in agreement with literature. Vortices are reproduced using a larger monopile which is represented with more cells in the mesh. This leads to the formation of ripples downstream of the monopiles and improves the simulation of the bed thickness evolution. Erosion of the bed and suspended sediment concentration are in agreement with the simulated bed shear stress simulated. The deposits of resuspended sediment downstream of the monopile is well represented because of the use of a sediment transport module which solves advection-diffusion equations. Regional modelling using four monopiles shows that the modifications of hydrodynamics due to monopile foundation of wind turbine can reach the foundation located downstream and interactions between monopile could be observed. However the relative decrease of velocity due to the first monopile is equal to 6 % close to the second monopile located downstream during the flow at medium tide. The dry points approach introduces a discontinuity and instabilities in the model which lead to asymmetry in velocity fields. This problem is not present with the parametrisation method which solves it.

Modelling of turbulence could be improved close to the monopile to better represent vortices and especially the horseshoe vortex. A morphological module is needed to take into account modifications of bathymetry around monopiles and better estimate the bed shear stress, and the effect of waves on the monopile impacts could be considered by coupling the circulation model MARS3D with the sea state model WW3 [5].

VI.5   Acknowledgments

References

[1] Achenbach, E., 1968. Distribution of local pressure and skin friction around a circular cylinder in cross-flow up to Re= 5×10^6. Journal of Fluid Mechanics 34 (04), 625–639.

[2] Actimar, 2013. Synthèse de l'étude 2009 - Analyse des impacts hydrosédimentaires du projet de parc éolien en mer en Baie de Seine,rapport moc n0732 prepared for Eoliennes offshore du Calvados.

[3] Baelhaq, A., 2014. Traitement des donnes expérimentales sur la synchronisation d'alle de Von Karman par les ondes superficielles. Master's thesis, Universit de Caen Basse-Normandie.

[4] Baptist, M., Babovic, V., Rodríguez Uthurburu, J., Keijzer, M., Uittenbogaard, R., Mynett, A., Verwey, A., 2007. On inducing equations for vegetation resistance. Journal of Hydraulic Research 45 (4), 435–450.

[5] Bennis, A.-C., Ardhuin, F., Dumas, F., 2011. On the coupling of wave and three-dimensional circulation models: Choice of theoretical framework, practical implementation and adiabatic tests. Ocean Modelling 40 (3), 260–272.

[6] Bouma, T., Van Duren, L., Temmerman, S., Claverie, T., Blanco-Garcia, A., Ysebaert, T., Herman, P., 2007. Spatial flow and sedimentation patterns within patches of epibenthic structures: Combining field, flume and modelling experiments. Continental Shelf Research 27 (8), 1020–1045.

[7] CEFAS, 2006. Scroby Sands Offshore Wind Farm - Coastal Processes Monitoring. Final Report AEO262 prepared for Marine Environmental Division, Defra and Department of Trade and Industry.

[8] Christie, E., Li, M., Moulinec, C., 2012. Comparison of 2d and 3d large scale morphological modeling of offshore wind farms using hpc. Coastal Engineering Proceedings 1 (33), sediment–42.

[9] Dargahi, B., 1989. The turbulent flow field around a circular cylinder. Experiments in Fluids 8 (1-2), 1–12.

[10] Department of Energy and Climate Change, 2008. Review of Round 1 sediment process monitoring data - lessons learnt, Final Report.

[11] DHI, 1999. Horns Rev Wind Power Plant. Environmental impact assessment of hydrography. Report prepared for ELSAMPROJEKT.

[12] Dixen, M., Lohmann, I. P., Christensen, E. D., 2012. Method to predict long time span of scour around offshore wind turbine foundations. Coastal Engineering Proceedings 1 (33), sediment–88.

[13] Jensen, M. S., Juul Larsen, B., Frigaard, P., DeVos, L., Christensen, E. D., Asp Hansen, E., Solberg, T., Hjertager, B. H., Bove, S., 2006. Offshore wind turbines situated in areas with strong currents. Tech. rep., Offshore Center Danmark.

[14] Kirkil, G., Constantinescu, S., Ettema, R., 2008. Coherent structures in the flow field around a circular cylinder with scour hole. Journal of Hydraulic Engineering 134 (5), 572–587.

[15] Lambkin, D., Harris, J., Cooper, W., Coates, T., 2009. Coastal process modelling for offshore wind farm environmental impact assessment: best practice guide. COWRIE Limited, London.

[16] Lazure, P., Dumas, F., 2008. external–internal mode coupling for a 3D hydrodynamical model for applications at regional scale (MARS). Advances in Water Resources 31 (2), 233–250.

[17] Le Hir, P., Cayocca, F., Waeles, B., 2011. Dynamics of sand and mud mixtures: a multiprocess-based modelling strategy. Continental Shelf Research 31 (10), S135–S149.

[18] Liu, J., Chen, J., Black, T., Novak, M., 1996. E-ε modelling of turbulent air flow downwind of a model forest edge. Boundary-Layer Meteorology 77 (1), 21–44.

[19] Navitus Bay Development Limited Ltd, 2014. Environmental statement, Volume B-Offshore, Chapter 5-Physical Processes, Document 6.1.2.5.

[20] O'Donncha, F., Hartnett, M., Nash, S., 2013. Physical and numerical investigation of the hydrodynamic implications of aquaculture farms. Aquacultural Engineering 52, 14–26.

[21] Rennau, H., Schimmels, S., Burchard, H., 2012. On the effect of structure-induced resistance and mixing on inflows into the Baltic Sea: A numerical model study. Coastal Engineering 60, 53–68.

[22] Roc, T., Conley, D. C., Greaves, D., 2013. Methodology for tidal turbine representation in ocean circulation model. Renewable Energy 51, 448–464.

[23] Roulund, A., Sumer, B. M., Fredsøe, J., Michelsen, J., 2005. Numerical and experimental investigation of flow and scour around a circular pile. Journal of Fluid Mechanics 534, 351–401.

[24] Sanz, C., 2003. A note on k-ε modelling of vegetation canopy air-flows. Boundary-Layer Meteorology 108 (1), 191–197.

[25] Temmerman, S., Bouma, T., Govers, G., Wang, Z., De Vries, M., Herman, P., 2005. Impact of vegetation on flow routing and sedimentation patterns: Three-dimensional modeling for a tidal marsh. Journal of Geophysical Research: Earth Surface (2003–2012) 110 (F4).

[26] Tseng, M.-H., Yen, C.-L., Song, C., 2000. Computation of three-dimensional flow around square and circular piers. International journal for numerical methods in fluids 34 (3), 207–227.

[27] Umlauf, L., Burchard, H., 2003. A generic length-scale equation for geophysical turbulence models. Journal of Marine Research 61 (2), 235–265.

[28] Vanhellemont, Q., Ruddick, K., 2014. Turbid wakes associated with offshore wind turbines observed with Landsat 8. Remote Sensing of Environment 145, 105–115.

VII

The Turbulent Wake of a Monopile Foundation

C. Rogan, J. Miles, D. Simmonds, G. Iglesias

VII.1 Introduction

Monopile foundations are by far the most common design for offshore wind turbines, comprising 91% of all European installations completed in 2014 [8]. They are well suited to shallow and transitional water depths, due to their simplicity of installation. At existing installations, piles are typically around 5 m in diameter. The UK is currently the world leader in terms offshore wind installed capacity, with further growth in the sector forming a key component of the government's renewables 2020 strategy [7].

As installations move into deeper water and turbine diameters increase, the greater horizontal loads and bending moments will necessitate the use of ever larger piles [5]. There are plans for turbines of 6 MW capacity, in as much as 30 m of water depth. Such installations will require monopiles of up to 7.5 m diameter [2]. With a greater number of ever larger monopiles anticipated in the coming years, it is important that we understand their impact.

The flow structure close to the base of a monopile has already been extensively studied [6, 9, 14, 15]. Three distinct flow structures can be identified close to the base of the pile. A horseshoe vortex forms at the upstream face, contraction of streamlines occurs as the flow accelerates around the sides of the pile, and lee wake vortices are formed immediately downstream of the pile.

In addition to the flow structures described above, the monopile's presence will cause increased turbulence in the flow downstream. Elevated turbulence enhances the carrying capacity of the flow, leading to increased sediment transport [4, 10]. This increases the distance that scoured sediments can be transported downstream of the pile. The environmental impacts of suspended sediments are numerous. Increased turbidity can affect the productivity of plankton [11], as well as influencing the behaviour of predatory fish [1] and marine mammals [17]. These are related to economic concerns, as any changes could impact on fisheries. Sediment transport regimes also govern sedimentation processes downstream [18].

This paper presents the results of a series of laboratory experiments examining the wake structure downstream of a monopile foundation. In particular, the influence on turbulence of flow velocity, pile diameter and location relative to the pile were measured. Empirical relationships are presented predicting the turbulent characteristics of the wake. Two new parameters are introduced to simplify turbulence assessment of planned monopile structures in terms the relative position and flow velocity.

VII.2 Materials and Methods

VII.2.1 Experimental Design

The experimental program was carried out in the Coastal basin at Plymouth University. The basin measures 10 m long by 7.2 m wide, with a water depth of 0.5 m. The pile was fixed to the floor of the basin, centred 4.5 m from the downstream tank wall and 3.5 m from the side.

Prototype values of water depth, pile diameter and flow velocity were chosen based on typical values at existing wind farm sites. [12] provide information from several existing wind farms. Average monopile

diameter is just below 5 m, with the largest quoted at 6 m. Pile diameters are expected to increase in the future as development moves into deeper water. Peak current velocities range between 0.6 and 2.0 m/s, although the higher values in this range correspond to particularly shallow sites. The experimental program was designed to examine turbulence in the free stream flow, and so an intermediate depth prototype was considered more appropriate. This was confirmed by examination of proposed sites in the channel region, using the ANEMOC offshore windfarm database [3].

Prototype values were converted to model scale by applying Froude similitude at a scale of 1:50 to derive appropriate scale factors (λ). Measurements were made at four model velocities ($u_0 = 0.08$, 0.14, 0.18 and 0.24 m/s), and two model pile diameters ($D = 0.1$ and 0.2 m), in water depth d of 0.5 m. Table VII.1 summarises the prototype and model parameters used.

Table VII.1: Prototype vs Model parameters

Parameter	λ	Prototype	Model
d	50	25 m	0.5 m
D	50	5-10 m	0.1-0.2 m
$\bar{u}_0$	$\sqrt{50}$	0.6-1.6 m/s	0.08-0.24 m/s

To allow comparison of results with different prototype scales, x and y positions in the tank were normalised by the pile diameter to yield x^* and y^*:

$$x^* = \frac{x}{D} \qquad y^* = \frac{y}{D}$$

VII.2.2 Data

Three components of velocity were measured using a Nortek Vectrino profiler Acoustic Doppler Velocimeter (ADV), referred to here as 'ADV1'. Detailed velocity measurements were made downstream of the model pile under steady flow conditions, with the goal of parameterising the wake structure. Velocity time series data were recorded using ADV1 positioned along transverse and longitudinal wake profiles (Figure VII.1). The longitudinal profile extended 2.7 m downstream of the pile centre, with nine measurement positions spaced logarithmically along its length. The eight transverse profiles were aligned perpendicular to the mean flow. Each profile extended 50 cm either side of the wake centreline.
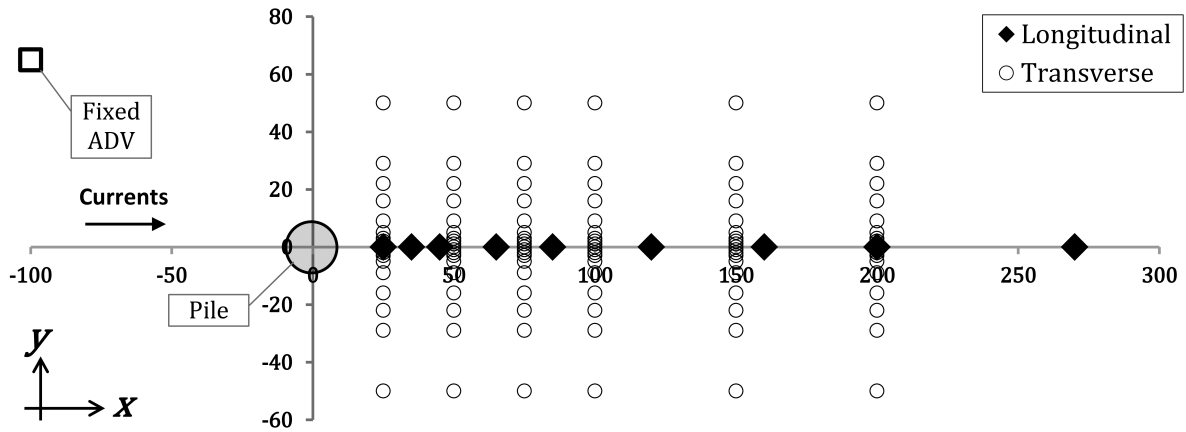

Figure VII.1: Experimental setup: plan view showing longitudinal and transverse measurement profiles. All dimensions in cm.

At each location, 500 seconds of velocity time series data was recorded at a sample frequency of 64 Hz, for each flow condition. The instrument was positioned vertically so that its sample volume was within the free stream, 35 cm from the tank floor. Velocity time series data from ADV1 was used to calculate Turbulent Kinetic Energy per unit volume (TKE), using equation 1.

$$TKE = \frac{1}{2}\rho(\bar{u'^2} + \bar{v'^2} + \bar{w'^2}) \tag{VII.1}$$

53

Where u, v and w are the components of velocity in the x, y and z directions, respectively, and the apostrophe indicates the fluctuating component. ρ is the density of water. Undisturbed flow was measured by a second ADV ('ADV2') positioned upstream of the pile.

VII.2.3   New Parameters

In assessing the environmental impact of a proposed monopile foundation, a fundamental consideration is the increase in turbulence relative to the ambient level in the undisturbed flow (TKE_0). To this end, a new parameter is introduced to express the increased turbulence in the pile wake - the Relative Excess Turbulence (RET):

$$RET = \frac{TKE - TKE_0}{TKE_0} \tag{VII.2}$$

Another useful parameter for impact assessment is the spatial extent of the pile's region of influence. A second new parameter is introduced to simplify comparisons between proposed installations. The Turbulence Recovery Lengthscale (TRL) is defined as the normalised distance required downstream, along the wake centreline, for turbulence to recover. Recovery can be considered to have taken place when RET falls below a threshold (Δ).

$$TRL = x^*$$

when

$$y^* = 0 \qquad \text{and} \qquad RET = \Delta$$

VII.3   Results

VII.3.1   Longitudinal Characteristics

Figure 2 shows measured TKE values along the centreline of the wake downstream of the 10 cm pile, at each of the three current velocities tested. Turbulence decays exponentially with distance downstream of the pile in all three datasets. As expected, higher mean flow velocity correlates with higher values of TKE. Similar trends were observed downstream of the 20 cm pile.
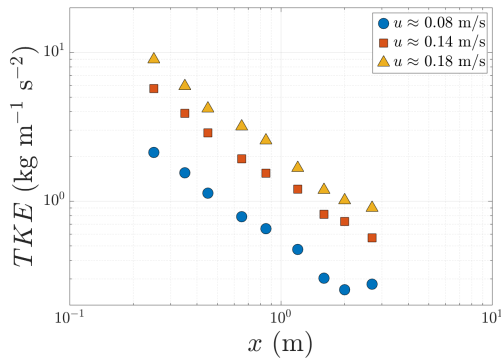

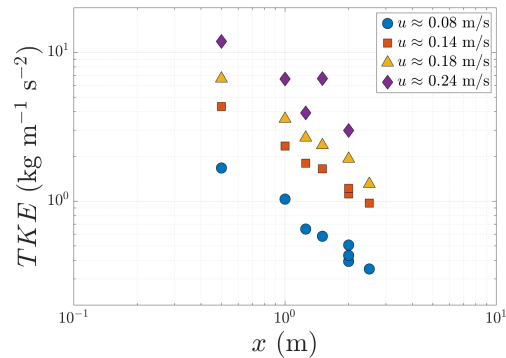Figure VII.2: Longitudinal TKE profiles: 10 cm diameter pile.

Figure VII.3: Longitudinal TKE profiles: 20 cm diameter pile.

TKE and x can be normalised by u_0 and D respectively. Data for both pile diameters and all four mean flow velocities collapsed towards a common relationship (Figure VII.4). Equation VII.3 fits the normalised data with an r^2 of 0.944. This shows that turbulence characteristics downstream of the pile centreline can be estimated using only $\bar{u}_0$ and D, parameters that will be known at an early design stage.

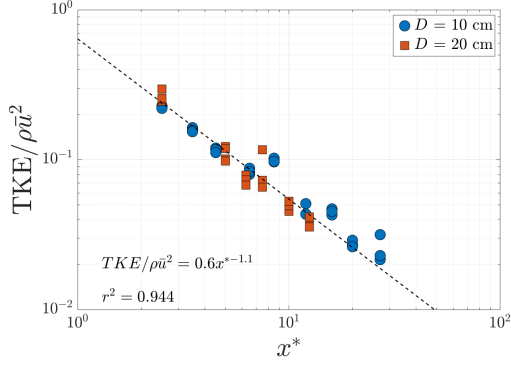$$\frac{TKE}{\rho \bar{u}_0{}^2} = 0.6x^{*-1.1} \tag{VII.3}$$

Figure VII.4: Normalised TKE longitudinal profiles. $\bar{u}_0 = 0.08$ to 0.18 m/s
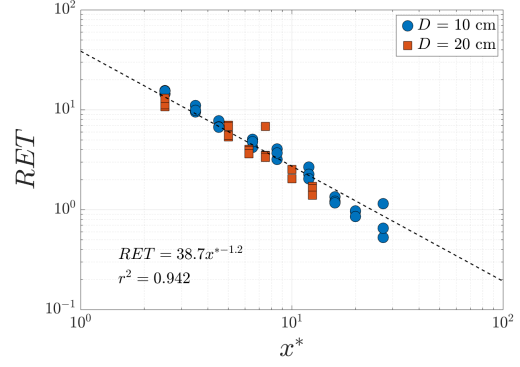

Figure VII.5: RET longitudinal profiles. $\bar{u}_0 = 0.08$ to 0.24 m/s

The wake TKE data from ADV1 was combined with undisturbed velocity data from ADV2, to calculate RET (equation VII.2). When this was applied, data for both pile diameters and all four mean flow velocities collapsed to a single relationship (Figure VII.5). Equation VII.4 fits the RET data with an r^2 value of 0.942.

$$RET = 38.7x^{*-1.2} \tag{VII.4}$$

VII.3.2   Transverse Characteristics

Figure VII.6 shows a typical transverse profile of normalised TKE. Normalised TKE was greatest along the wake's centreline, and rapidly dropped to a constant background value on either side. Transverse TKE cross sections collapsed when normalised by mean $\rho \bar{u}_0^2$ and D, as was the case with the longitudinal profiles.
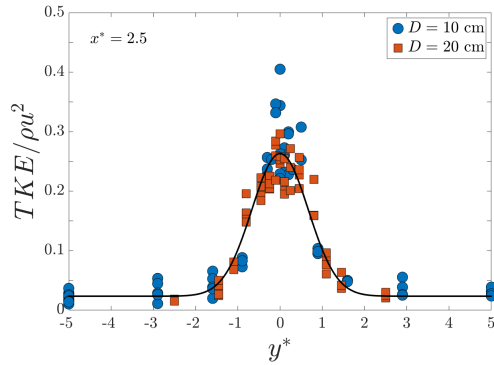

Figure VII.6: Normalised TKE cross section, 2.5 D downstream. Data for different velocities and pile diameters collapsed to a common relationship.
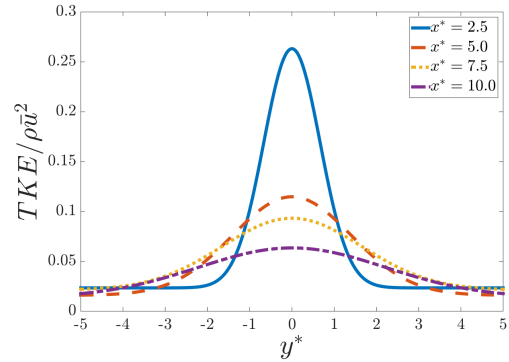

Figure VII.7: Transverse profiles fitted to normalised TKE data at four different values of x^*. Cross sections become lower and wider with x^*.

The distribution of TKE in the cross sections was found to fit a Gaussian distribution of the form:

$$\frac{TKE}{\rho \bar{u}_0^2} = \alpha_1 e^{-\alpha_2 y^{*2}} + \alpha_3 \tag{VII.5}$$

Where α_1, α_2 and α_3 are regression constants. Non-linear regression was used to determine the values of these constants for each of the four y^* profiles (Table VII.2).

For a given cross section, the peak value of TKE is governed by the constant α_1. Given the distance downstream and the pile diameter, the value of α_1 might be estimated using equation VII.4. Likewise,

55

Table VII.2: Regression constants for normalised TKE cross sections.

x^*	α_1	α_2	α_3	r^2
2.5	0.2397	1.1189	0.0234	0.9182
5.0	0.0988	0.2521	0.0160	0.7894
7.5	0.0719	0.1823	0.0213	0.5273
10.0	0.0497	0.1015	0.0138	0.5826
$Mean$	-	-	0.0186	0.7044

the width of the wake is governed by the constant α_2. Both constants tend towards zero as x^* increases and the wake profile becomes lower, wider and flatter (Figure VII.7).

Figure VII.8 plots RET against y^*, for ***two of the four values of x^* tested. Each plot represents two different pile diameters and four different flow velocities. As with the longitudinal profiles, the data collapses very well when normalised in this way. Peak RET occurs along the centreline. The shape of the wake becomes lower, flatter and wider as x^* increases.
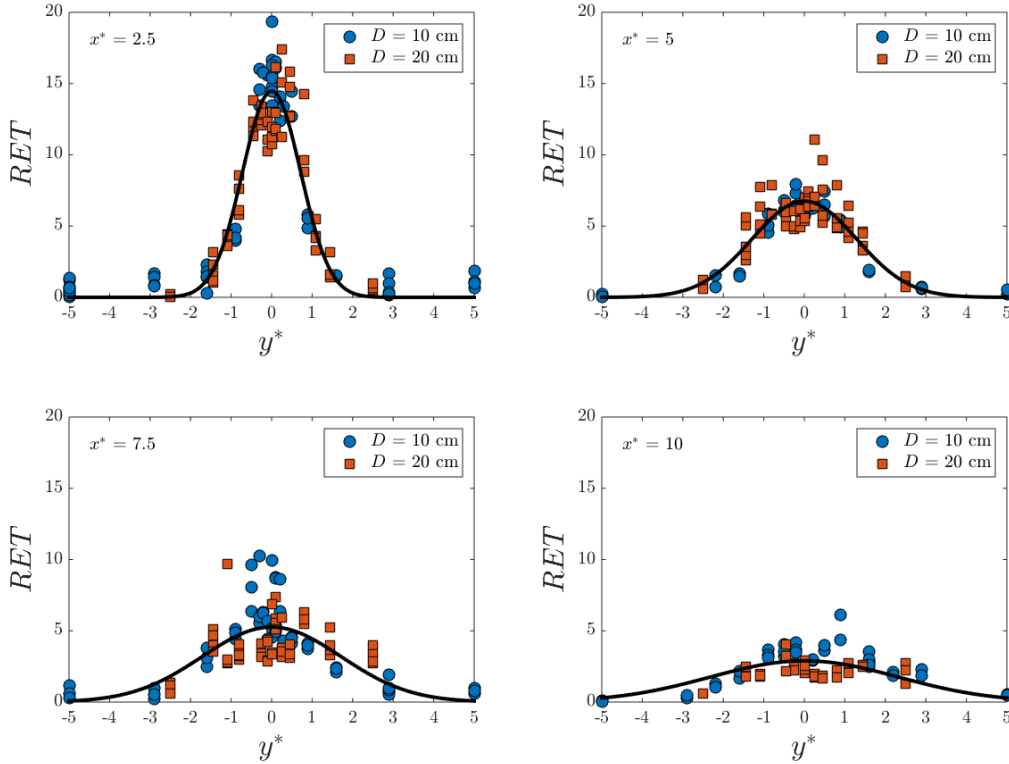

Figure VII.8: RET - transverse cross sections at different values of y^*. Black lines indicate equation VII.6 fitted to the measured data. Profiles become lower, flatter and wider as y^* increases.

RET values recover to approximately zero at the boundaries of the wake. This allows equation VII.5 to be simplified to give equation VII.6:

$$RET = \beta_1 e^{-\beta_2 y^{*2}} \qquad \text{(VII.6)}$$

Table VII.3 summarises the fitting of experimental data to this relationship. As with Table VII.2, the values of the constants tend towards zero as x^* increases. Comparing r^2 values between the two tables, the RET fits are slightly better close to the pile, but slightly poorer further away.

Figure VII.8 suggests that equation VII.6 reliably fits the crest of the dataset for each profile. The reduction in r^2 values with x^* appears to be due to larger residuals close to the wake boundaries.

Table VII.3: Regression constants for RET cross sections.

x^*	β_1	β_2	r^2
2.5	14.2265	0.9479	0.9331
5.0	6.7503	0.2999	0.8327
7.5	5.2612	0.1703	0.5215
10.0	2.8917	0.0928	0.4760
$Mean$	-	-	0.6908

VII.3.3 Empirical Model

Following the observations made in sections ** and **, a unifying relationship was sought to describe the distribution of turbulence over the entire domain. The validity of such a relationship follows from dimensional analysis of the parameters. Combining equations VII.4 and VII.6 yields a relationship of the form:

$$RET = \gamma_1 x^{*-\gamma_2} e^{-\frac{\gamma_3 y^{*2}}{x^*}} \tag{VII.7}$$

Using non-linear regression, the measured data was fit to equation VII.7, yielding the following constants:

$$\gamma_1 = 34.601 \qquad \gamma_2 = 0.9796 \qquad \gamma_3 = 2.0552$$

Figure VII.9 plots the measured data over the entire domain, against a surface defined by equation 7 and the fitted values of γ_1, γ_2 and γ_3. The function was found to fit measured data with an r^2 of 0.87. The function successfully explains both the exponential decay of RET along the wake centreline and the spreading of the wake with distance downstream.

VII.3.4 Outputs

Equation VII.7 allows the calculation of TRL along the wake centreline. By setting y^* equal to zero and RET equal to Δ, γ_3 is eliminated and the equation simplifies:

$$\gamma_1 x^{*-\gamma_2} = \Delta \tag{VII.8}$$

$$x^* = e^{\frac{ln\frac{\gamma_1}{\Delta}}{\gamma_2}} = TRL \tag{VII.9}$$

The value of the threshold Δ is arbitrary, and different values may be specified according to the purpose of the analysis. Two examples serve to illustrate this point. Given a receptor or process that is insensitive to variations in turbulence, Δ might be set equal to 1.0. This yields a value of 37.20 for TRL, or approximately 40, corresponding to a distance of 200 m for a typical 5 m diameter prototype. This is not expected to be significant on a regional scale.

If instead the process of interest is highly sensitive to changes in turbulence, Δ might be set at 0.1. This implies that TKE has decayed to only 10% above the ambient conditions - a much tighter specification than above. Using this new threshold TRL is calculated at 389.8, or approximately 400 - corresponding to 2000 m downstream for a typical 5 m diameter prototype.

VII.4 Discussion

The findings indicate that turbulence affects a substantial region downstream of the pile, showing that turbulence is a much larger scale problem than scour. Changes to the turbulent characteristics of the flow may be significant for mixing, and could affect primary productivity and marine biodiversity in the region of the pile [11]. This is in good agreement with the findings of [16], who reported turbid plumes 30 to 150 m wide, extending for several km downstream of wind farms. Translating RET values into quantities of suspended particulate matter would require data on the characteristics of the suspended material and the ambient conditions at a specific site, as proposed by [13]. However, heightened TKE at this distance from the pile will enhance the carrying capacity of the flow, and contribute to the persistence of the observed plumes.
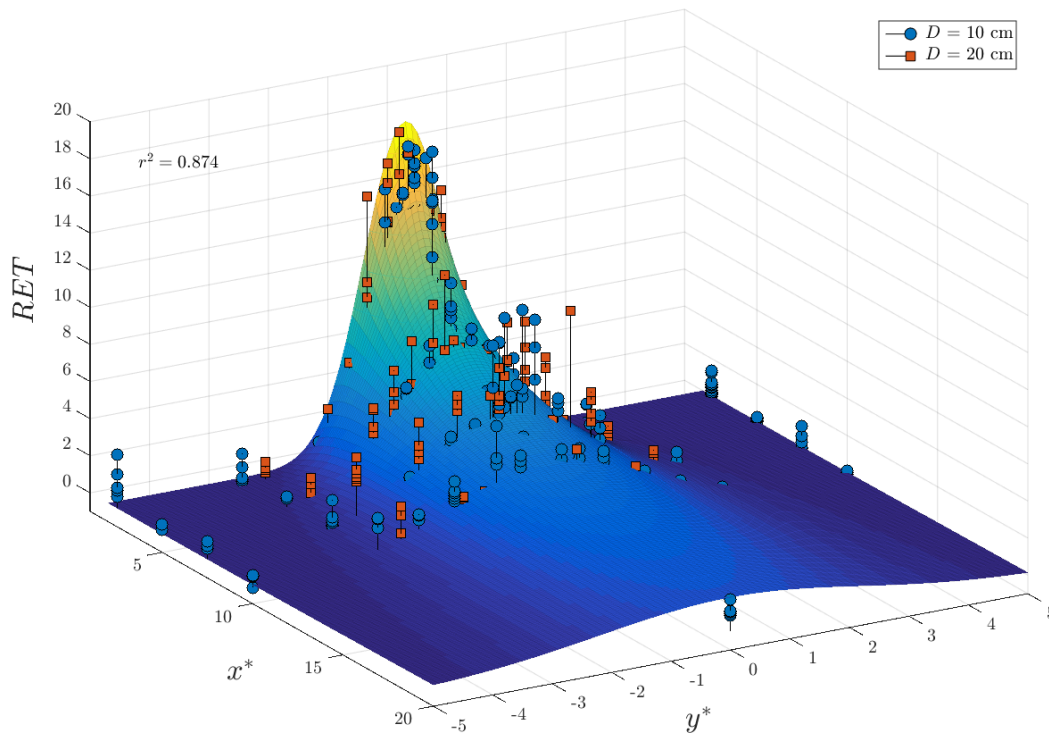
Figure VII.9: Distribution of Residual Excess Turbulence (RET), against normalised distance downstream (x^*) and off axis (y^*) from the pile centre. Measured values against a surface defined by equation VII.7.

Prototype pile spacing within a wind farm is typically 500 to 1000 m, with pile diameters around 5 m. Given these values, the estimated TRL values imply that the RET reaching downstream monopiles will be somewhere between 1.0 and 0.1. When compared to the initial RET values of 34.6 at $x^* = 1.0$ (equation VII.7), this suggests that any cumulative effect within a wind farm will be negligible.

VII.5   Conclusion

A detailed experimental program was carried out in a laboratory to assess the levels of turbulence in the wake of a monopile foundation. Turbulence along the wake centreline was found to decay exponentially with distance downstream. Turbulence introduced by the monopile was estimated to persist for approximately 400 pile diameters downstream.

In this work, two new parameters have been introduced for characterising the turbulence downstream of a monopile foundation: the Relative Excess Turbulence (RET) and the Turbulence Recovery Length-scale (TRL). These parameters will be useful for assessing the likely impact of monopile foundations on local flow conditions. TRL was estimated at 40 for an RET threshold of 1.0, or 400 for an RET threshold of 0.1.

Profiles of turbulence across the wake fitted a Gaussian function. The lateral extent of the pile's impact increased with distance downstream of the pile. Normalised TKE outside the wake was unaffected by the pile's presence.

VII.6   Acknowledgments

project was selected under the European cross-border cooperation programme INTERREG IV A France (Channel) - England, co-funded by the ERDF (European Regional Development Fund).

References

[1] Mark Abrahams and Michael Kattenfeld. The role of turbidity as a constraint on predatory-prey interactions in aquatic environments. *Behavioural Ecology and Sociobiology*, 40:169 – 174, 1997.

[2] M. Achmus, K. Abdel-Rahman, and Yu-Shu Kuo. Design of Monopile Foundations for Offshore Wind Energy Converters. In *11th Baltic Sea Geotechnical Conference*, Gdansk, 2008.

[3] Michel Benoit, Florence Lafon, and Gérard Goasguen. Constitution et exploitation d'une base de données d'états de mer le long des côtes françaises par simulation numérique sur 23 ans. *European Journal of Environmental and Civil Engineering*, 12(February 2015):35–50, 2008.

[4] Tony Butt, Paul Russell, Jack Puleo, Jon Miles, and Gerhard Masselink. The influence of bore turbulence on sediment transport in the swash and inner surf zones. *Continental Shelf Research*, 24:757–771, 2004.

[5] B W Byrne and G T Houlsby. Foundations for offshore wind turbines. *Philosophical Transactions of The Royal Society*, 361:2909–2930, 2003.

[6] B Dargahi. The turbulent flow field around a circular cylinder. *Experiments in Fluids*, 12:1–12, 1989.

[7] DECC. UK Renewable Energy Roadmap. Technical Report November, Department of Energy and Climate Change, 2013.

[8] EWEA. The European offshore wind industry - key trends and statistics 2014. Technical Report January, European Wind Energy Association, 2015.

[9] I García-Hermosa, J Brossard, Z Cohen, G Perret, G Pinon, N Abcha, A C Bennis, A Ezersky, D Mouazé, A Rivier, G Iglesias, J Miles, C Rogan, D Simmonds, M Gross, and V Magar. Experimental characterisation of wave induced flow fields due to an offshore wind farm mast. In *Proceedings of the 1st International Conference on Renewable Energies Offshore*, Lisbon, 2014.

[10] Albert Gyr and Klaus Hoyer. *Sediment Transport A Geophysical Phenomenon*. Springer, 2006.

[11] Esra Kocum, G. J C Underwood, and David B. Nedwell. Simultaneous measurement of phytoplanktonic primary production, nutrient and light availability along a turbid, eutrophic UK east coast estuary (the Colne Estuary). *Marine Ecology Progress Series*, 231:1–12, 2002.

[12] Clara Matutano, Vicente Negro, José-Santos López-Gutiérrez, M Dolores Esteban, and J María del Campo. Dimensionless wave height parameter for preliminary design of scour protection in offshore wind farms. *Journal of Coastal Research*, 29(65):1633–1638, 2013.

[13] A Rivier, A C Bennis, G Pinon, M Gross, and V Magar. Modelisation numerique regionale de l'impact des eoliennes offshore sur l'hydrodynamique et le transport sedimentaire. *Journées de l'hydrodynamique*, 14, 2014.

[14] BM Sumer, N Christiansen, and J Fredsøe. The horseshoe vortex and vortex shedding around a vertical wall-mounted cylinder exposed to waves. *Journal of Fluid Mechanics*, 332:41–70, 1997.

[15] Jens Unger and Willi H. Hager. Down-flow and horseshoe vortex characteristics of sediment embedded bridge piers. *Experiments in Fluids*, 42(1):1–19, November 2006.

[16] Quinten Vanhellemont and Kevin Ruddick. Turbid wakes associated with offshore wind turbines observed with Landsat 8. *Remote Sensing of Environment*, 145:105–115, April 2014.

[17] Michael Weiffen, Bettina Möller, Björn Mauck, and Guido Dehnhardt. Effect of water turbidity on the visual acuity of harbor seals (*Phoca vitulina*). *Vision Research*, 46:1777–1783, 2006.

[18] Yue Yin, Elizabeth Christie, Ming Li, Charles Moulinec, and David Emerson. 3d morphological impact modelling of offshore wind farms using les and hpc. *Coastal Engineering Proceedings*, 1(34):sediment–48, 2014.